AGU PUBLICATIONS

Tectonics

RESEARCH ARTICLE
10.1002/2016TC004440

Key Points:
- Isostatically compensated, balanced cross section linked to a thermokinematic model
- Basement thrust sheets set the first-order cooling pattern that matches measured ages in Bolivian Andes
- FTB deformation started at 50 Ma with peak shortening at ~50–45 Ma and ~12–8 Ma

Supporting Information:
- Supporting Information S1

Correspondence to:
A. J. Rak,
adamrakgeo@gmail.com

Citation:
Rak, A. J., McQuarrie, N., & Ehlers, T. A. (2017). Kinematics, exhumation, and sedimentation of the north central Andes (Bolivia): An integrated thermochronometer and thermokinematic modeling approach. *Tectonics*, *36*. https://doi.org/10.1002/2016TC004440

Received 15 DEC 2016
Accepted 12 OCT 2017
Accepted article online 18 OCT 2017

Kinematics, Exhumation, and Sedimentation of the North Central Andes (Bolivia): An Integrated Thermochronometer and Thermokinematic Modeling Approach

Adam J. Rak[1,2], Nadine McQuarrie[1], and Todd A. Ehlers[3]

[1]Department of Geology and Environmental Science, University of Pittsburgh, Pittsburgh, PA, USA, [2]Now at Rak Geologic Consulting LLC, Greenville, PA, USA, [3]Department of Geoscience, University of Tübingen, Tübingen, Germany

Abstract Quantifying mountain building processes in convergent orogens requires determination of the timing and rate of deformation in the overriding plate. In the central Andes, large discrepancies in both timing and rate of deformation prevent evaluating the shortening history in light of internal or external forcing factors. Geologic map patterns, age and location of reset thermochronometer systems, and synorogenic sediment distribution are all a function of the geometry, kinematics, and rate of deformation in a fold-thrust-belt-foreland basin (FTB-FB) system. To determine the timing and rate of deformation in the northern Bolivian Andes, we link thermokinematic modeling to a sequentially forward modeled, balanced cross section isostatically accounting for thrust loads and erosion. Displacement vectors, in 10 km increments, are assigned variable ages to create velocity fields in a thermokinematic model for predicting thermochronometer ages. We match both the pattern of predicted cooling ages with the across strike pattern of measured zircon fission track, apatite fission track, and apatite (U-Th)/He cooling ages as well as the modeled age of FB formations to published sedimentary sections. Results indicate that northern Bolivian FTB deformation started at 50 Ma and may have begun as early as 55 Ma. Acceptable rates of shortening permit either a constant rate of shortening (~4–5 mm/yr) or varying shortening rates with faster rates (7–10 mm/yr) at 45–50 Ma and 12–8 Ma, significantly slower rates (2–4 mm/yr) from 35 to 15 Ma and indicate the northern Bolivian Subandes started deforming between 19 and 14 Ma.

1. Introduction

The central Andean Cordillera is the modern archetype of a retroarc fold-thrust-belt-foreland basin (FTB-FB) system resulting from strain accumulated due to the westward motion of the South American plate over the subducting Nazca plate (Allmendinger et al., 1997; DeCelles, 2012; Jordan, 1995). Interest in the geodynamic evolution of FTB-FB systems stem from their intrinsic relationships with lithospheric deformation, crustal rigidity, convergent plate margin evolution, FB hydrocarbon deposits, and high topography that may influence atmospheric circulation and precipitation (Barnes & Ehlers, 2009; Coney & Evenchick, 1994; DeCelles, 2012; Ehlers & Poulsen, 2009; Jordan, 1981; Mount, 2014; Song et al., 2010; Stockmal et al., 2007). The distribution of sediment in hinterland and foreland basins of the Bolivian Andes is controlled by the spatiotemporal evolution of deformation in the Andean FTB (DeCelles & Horton, 2003; Jordan et al., 1997; McQuarrie et al., 2005; Sempere et al., 1990). While many studies attempt to quantify the age of initiation, magnitude of deformation, and rate of shortening, previous results are still contested due to the need for additional age constraints on the deformation history (Allmendinger et al., 1997; Armijo et al., 2015; Eichelberger & McQuarrie, 2015; Gillis et al., 2006; Horton et al., 2001; McQuarrie et al., 2008, 2005; Oncken et al., 2006).

Temporal aspects of deformation have previously been inferred through geochronology and provenance analyses of FB and wedge-top sediment, and bedrock thermochronometer data. Synorogenic sediment geochronology has been used to interpret the initiation of deformation in the Bolivian FTB. Initial studies proposed the original pulse of deformation in the FTB occurred in the Oligocene (38–25 Ma) based on the age of synorogenic wedge-top sedimentary rocks and cooling recorded in Triassic age plutons (Allmendinger et al., 1997; Farrar et al., 1988; Jordan et al., 1997; Lamb & Hoke, 1997; Lamb et al., 1997; Oncken et al., 2006; Sempere et al., 1997; Sempere et al., 1990). However, Maastrichtian through early Eocene (73–50 Ma) sedimentary rocks preserved in the Bolivian Altiplano have been interpreted as a part of an early FB system, driven by initial deformation in northern Chile and westernmost Bolivia in the Late Cretaceous (Coney & Evenchick, 1994; DeCelles & Horton, 2003; Horton, 2012; Horton et al., 2001). In addition, recent

thermochronometer analysis of K-feldspar $^{40}Ar/^{39}Ar$ (K-Fels), zircon fission track (ZFT), and apatite fission track (AFT) systems from the Triassic age plutons indicate rapid cooling occurred in the Eocene (45–40 Ma) and have been use to argue for early Eocene deformation-induced exhumation (Barnes et al., 2012; Benjamin et al., 1987; Gillis et al., 2006; McQuarrie et al., 2008).

Deformation rates are dependent upon when deformation initiates as well as shortening magnitude. Magnitudes of total shortening determined through balanced cross-section analyses of the central Andean FTB range from ~200 to 400 km (Baby et al., 1995, 1997; Eichelberger & McQuarrie, 2015; Gotberg et al., 2010; Kley, 1996; McQuarrie, 2002a; McQuarrie et al., 2008; Müller et al., 2002; Sheffels, 1990). While the total amount of shortening and age of initial deformation provide a long-term rate of shortening, it is also likely that the rate of shortening through the central Andes has varied with time (Echavarria et al., 2003; McQuarrie et al., 2008, 2005; Oncken et al., 2006). The large discrepancies in proposed age, magnitude, and rate of deformation prevent the accurate characterization of the shortening history of this retroarc FTB-FB system, or relating that shortening history to internal or external forcing factors (DeCelles et al., 2009; Hindle et al., 2002; Iaffaldano et al., 2006; McQuarrie, 2002b; Meade & Conrad, 2008).

In this study, we build on decades of structural and geochronologic studies of the region and contribute a sequentially deformed, isostatically balanced, thermokinematic model of the northern Bolivian Andes between 15 and 17°S to quantitatively link the geometric, kinematic, erosional, and sedimentary evolution of a retroarc FTB that can be used to assess proposed geodynamic forcing factors for Andean Plateau. This transect across the central Andes is chosen based on the concentration of published cooling ages for a suite of different thermochronometers, dated FB stratigraphy and preserved wedge-top basins and an existing cross section based on detailed geologic mapping. We evaluate permissible ranges in the age of initiation and rate of deformation through forward kinematic modeling of a cross section through northern Bolivia (McQuarrie et al., 2008) to both reproduce particle paths of exhumed, previously published, thermochronometer data in the FTB and predict the location, age, and thickness of foreland and hinterland basins. We understand that shortening rates as well as the loci of erosion, cooling, and sedimentation are strongly dependent on the proposed cross-section geometry, and thus, different modeled cross sections may produce varying estimates for age and rate of deformation. However, we present this approach as a mechanism for testing the validity and applicability of a given structural model and, in doing so, evaluate this models ability to match the measured data. This combined modeling technique identifies relationships between FTB thermochronometry and synorogenic sediment data sets and illustrates the effects of structural geometry, kinematics, erosion, isostasy, and thermal controls on Central Andean mountain belt formation over the past 55 Ma.

2. Geologic Setting

2.1. The Central Andes

The central Andes reaches elevations of 4 to >6 km with crustal thicknesses up to 60–70 km (Beck et al., 1996; Ryan et al., 2016) and records the highest shortening magnitudes along the ~8000 km long Andean mountain chain (Allmendinger et al., 1997; Barnes & Ehlers, 2009; Kley & Monaldi, 1998; Kley et al., 1999; McQuarrie, 2002b). The central Andes are home to the Andean plateau, defined as the high elevation (>3 km) region encompassing the Western Cordillera, Altiplano, and the Eastern Cordillera (Allmendinger et al., 1997; Isacks, 1988; Lamb & Hoke, 1997). The Western Cordillera (WC) active volcanic arc reaches elevations >6 km along the Pacific-Altiplano (AP) drainage divide (Allmendinger et al., 1997; Isacks, 1988). The Altiplano (AP) is a low-relief, high-elevation (~3.7 km) internally drained basin that has collected up to 12 km of Tertiary sedimentary rocks (Horton et al., 2001, 2002). The bivergent, hinterland component of the Andean FTB defines the Eastern Cordillera (EC) with elevations that reach 6.4 km. The EC contains thrusts that root in lower Paleozoic strata producing narrow (5 km wide) anticlines and synclines that commonly include concordant Mesozoic and early Cenozoic rocks (Horton, 2005; McQuarrie, 2002a; McQuarrie & DeCelles, 2001). The Interandean zone (IAZ) is a region of tightly folded, predominantly Paleozoic units that is characterized by a significant decrease in topographic and structural elevation compared to the EC (Kley, 1996; McQuarrie, 2002a). The Subandean zone (SAZ) is the actively deforming FTB characterized by long (10–20 km) thrust sheets of Paleozoic through Tertiary rocks that produce synclines preserving 4–7 km of Cenozoic synorogenic sediment (Baby et al., 1995; Dunn et al., 1995; Rodriguez & Fernando, 2002).

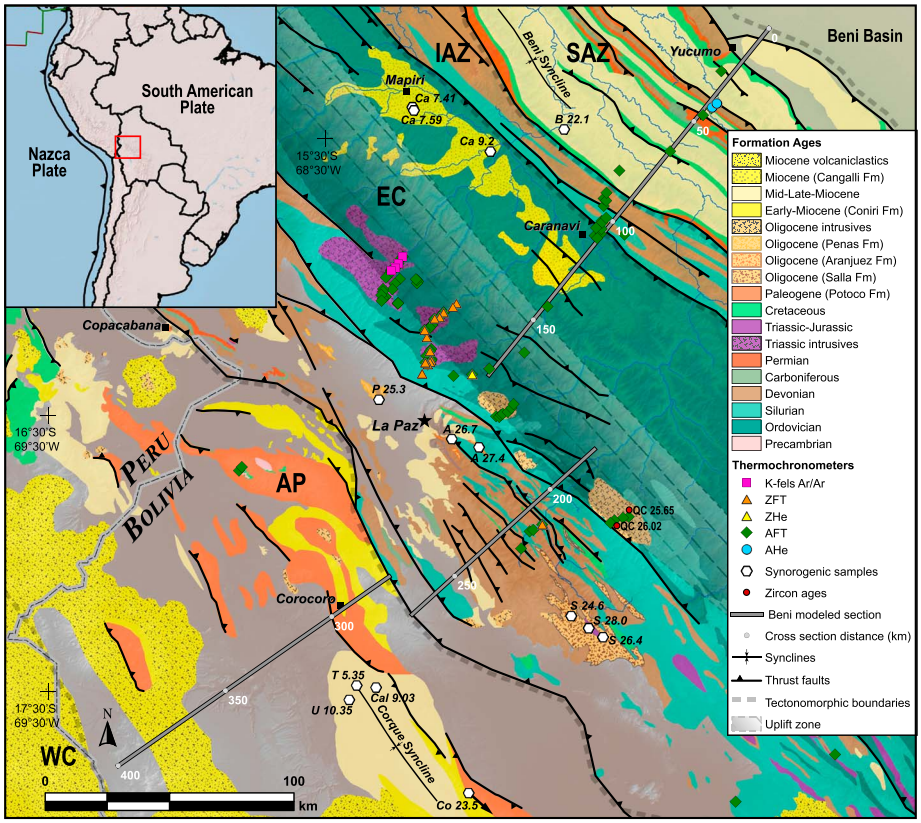

Figure 1. Geologic map of northern Bolivian Andes with formation ages based on McQuarrie et al., 2008 (Kennan et al., 1995; Geobol, 1994a, 1994b, 1995a, 1995b, 1996, 1997; Horton et al., 2001; McQuarrie et al., 2008); published thermochronometers (Barnes et al., 2012, 2006; Benjamin et al., 1987; Gillis et al., 2006; Kay et al., 1998; Lease et al., 2016; MacFadden et al., 1985; Marshall et al., 1992; McQuarrie et al., 2008; Safran et al., 2006); published geochronometers (Gillis et al., 2006; Kennan et al., 1995; Leier et al., 2010; Mosolf et al., 2011; Murray et al., 2010); the Beni modeled cross section with distances from foreland, synclines, significant thrust faults, boundaries between tectonomorphic zones, and zone of uplift as determined by geomorphic indices (Whipple & Gasparini, 2014), draped over a hill shaded 30 m pixel resolution digital elevation model (DEM) in WGS 1984. Tectonomorphic zone from west to east: Western Cordillera (WC); Eastern Cordillera (EC); Interandean Zone (IAZ); Subandean Zone (SAZ). Synorogenic sediment geochronometer samples are labeled by age (Ma) and formation: A, Aranjuez Formation; B, Beni Syncline; Ca, Cangalli Formation; Cal, Callapa tuff; Co, Coniri Formation; P, Penas Formation; S, Salla Formation; T, Toba 76 tuff; and Ulloma tuff. Zircon U/Pb sample form Oligocene plutons in the central EC are from the Quimsa Cruz granite (QC) and are labeled by age (Ma). Inset shows the location of the study area in relation to plate boundaries and South American country boundaries.

The Beni basin is the actively accumulating FB with up to 4–5.5 km of Cenozoic sediment (Horton & DeCelles, 1997; Zubieta Rossetti et al., 1996) (Figure 1).

2.2. Shortening Estimates and Geometry

Many of the early estimates of shortening through the central Andes focused on the eastern portion of the system in the IAZ and SAZ (Baby et al., 1997; Kley, 1996; Kley & Monaldi, 1998). Later studies that produced detailed geologic maps and resulting cross sections through the entire Cordillera, particularly including the west verging backthrust belt, substantially increased the documented shortening magnitudes (Eichelberger et al., 2013; McQuarrie, 2002a; McQuarrie et al., 2008; McQuarrie & DeCelles, 2001; Müller et al., 2002; Sheffels, 1990).

The critical structures that need to be matched by any cross section through this portion of the central Andes are (1) broad, large wavelength (10–20 km) and deep 6.5–7 km synclinal basins separated by narrow zones (1–5 km wide) of thrust-faulted anticlines (Baby et al., 1995; McQuarrie et al., 2008) in the SAZ; (2) rapid increase in structural elevation (~12 km) in the IAZ in conjunction with closely spaced (3–10 km) but small displacement (1–5 km) thrust faults that carry Paleozoic rocks and folds with wavelengths of 3–5 km (McQuarrie et al., 2008); (3) folded Ordovician rocks throughout the EC with wavelengths of 1 km or less

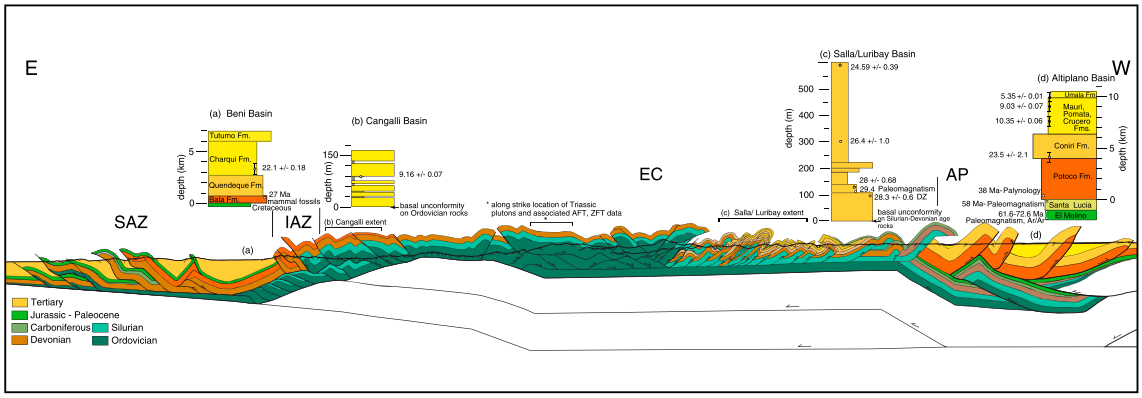

Figure 2. Balanced cross section through the Andean fold-thrust belt in Northern Bolivia (from McQuarrie et al., 2008). The line of section is shown in Figure 1 and supporting information Figure SI 1. Note that structures and their accompanying stratigraphy are projected above topography (heavy black line) to indicate amount of displacement through erosion surface. The stratigraphic sections for wedge-top, foreland, and hinterland basins and the associated geochronology that are used to constrain age of deformation are shown above and adjacent to their locations on the cross section (a) Beni Basin, (b) Cangalli Basin, (c) Salla/Luribay Basin, and (d) Altiplano Basin. Geochronologic references are provided in the text and supporting information (section S5).

on the eastern side and a gently folded, undulating upper Ordovician surface that is broken by a few low offset (0.5–2 km) faults on the western side; the amplitude of folding is 1–2 km with wavelengths of 10 km; (4) closely spaced faults (2–5 km) in the western EC with 2 to up to 12 km of displacement that systematically repeat the Silurian through Devonian section and verge westward toward the Altiplano (Figure 2); the close spacing, narrow wavelength and repeating lithologic package requires a relatively shallow (with respect to the rocks at the surface), uniform decollement horizon; and (5) a 12 km stratigraphic separation between the west verging backthrust belt and the Tertiary sedimentary rocks preserved in the Altiplano. The balanced cross section by McQuarrie et al. (2008) argues that the shortening accommodated by the multiple faults and tightly spaced folds in Silurian to Devonian rocks in the backthrust belt (~120 km) is balanced by equal amounts of shortening in duplexed Ordovician rocks immediately to the east producing the mapped, gently folded, undulating surface of upper Ordovician strata in the overlying roof thrust (Figure 2). This geometry allows slip on the duplex to be transferred to faults within the Silurian and younger strata in the back thrust belt to the west, so that the total amount of shortening throughout the stratigraphic section is equal.

The pronounced changes in structural elevation between the SAZ, IAZ, EC, and AP are imaged in geophysical surveys of the region (e.g., Ryan et al., 2016) and have always been interpreted as a function of basement thrust sheets in crustal-scale cross sections (Baby et al., 1997; Kley, 1996, 1999; Kley et al., 1996; McQuarrie, 2002a; McQuarrie et al., 2008; McQuarrie & DeCelles, 2001; Müller et al., 2002). The notable difference between these cross section interpretations is the thickness, geometry, and vergence of the basement thrusts (e.g., Baby et al., 1997; McQuarrie, 2002a; Müller et al., 2002). Baby et al. (1997) show basement thrust faults, ~20 km thick that repeat the entire basement package in a series of eastward verging and eastward younging faults. The interpretation of Müller et al. (2002) is more complicated with basement faults that range in thickness from 8 to 15 km and verge both to the east (in the eastern EC and IAZ) and west (western EC). McQuarrie (2002a) argued for two large (~10–12 km thick) east verging basement thrust sheets that used the brittle ductile transition zone (where the strength contrast in the crust is the largest) as a midcrustal detachment, a concept originally proposed by Hatcher and Hooper (1992) for crystalline thrust sheets.

Again, for balance, the shortening accommodated by these basement thrusts must equal the amount of shortening accommodated by faulting of sedimentary rocks exposed at the surface (as defended by the match between the proposed cross section structures and the structures identified in geologic maps) (supporting information Figure SI 1). We contend that the size of these proposed basement structures (8–20 km thick) and their first-order control on the pronounced changes in structural elevation in the Andes (i.e., the depth to which rocks are erosionally exhumed, exposing lower Ordovician rocks in the EC and Devonian through upper Silurian in the IAZ) strongly suggest that they should also exert a first-order control on the cooling history of the overlying rocks. Thus, the viability of basement structures can be evaluated by comparing the predicted age and distribution of thermochronometers imparted by the structures geometry

and kinematics to measured ages through the region. For this study, we use the cross section of McQuarrie et al. (2008) because of its colocation with a comprehensive suite of published cooling ages and well-dated foreland and wedge-top basin sedimentary rocks to evaluate the control the proposed basement structures exert on the cooling ages and the location and age of synorogenic sedimentation.

2.3. Cenozoic Foreland and Hinterland Basin Deposits

Synorogenic sediments were deposited on top of undeformed Paleozoic and Mesozoic rocks in the Altiplano and Beni basins throughout the Cenozoic in conjunction with FTB deformation (DeCelles & Horton, 2003; Horton, 2005; Horton et al., 2001; McQuarrie et al., 2005) (Figure 2). Early Tertiary sedimentation in the AP consisted of ~1–2 km of mostly nonmarine mudrock, sandstone, and carbonate lithologies deposited in distal fluviolacustrine systems (Horton et al., 2001, 2002; Kennan et al., 1995). Separated from this lower section by a thick layer of paleosols, the late Eocene-Oligocene Potoco Formation (3–6 km) records a paleocurrent direction initially from eastward directed channel systems draining the WC to both east and to west directed systems in the upper portions of the formation (Hampton & Horton, 2007). The basin forming mechanism for these early Tertiary rocks is proposed to be a flexurally induced backbulge, forebulge, and foredeep due to the evolution and eastward migration of a Paleogene FTB located west of the Altiplano (DeCelles & Horton, 2003; Horton, 2005; Horton et al., 2001, 2002). The Miocene age Coniri Formation (and equivalents; ~3 km) is dominated by sediments from the east, indicating the significant sediment source was focused in the EC (Horton et al., 2001, 2002). Sedimentation continued through the late Miocene depositing 1–4 km thick sandstones, conglomerates, and volcaniclastic rocks (Garzione et al., 2006). The entire Cenozoic package is approximately 12 km thick and represents a proposed foreland to hinterland basin sequence that preserved sediment derived from deformed rocks on the western and eastern flanks of the AP. Age constraints in this basin are sparse for the early history. A biotite geochronology age from an interbedded tuff sample was collected in the eastern limb of the Corque Syncline from the eastern derived Coniri Formation (Kennan et al., 1995). The sample yielded two biotite K-Ar/Ar ages (23.9 ± 1.3 Ma and 23.0 ± 0.8 Ma) that are projected along the Corque Syncline to the Beni modeled section (Figure 1, label Co 23.5). The late Miocene tuffaceous sandstones and mudstones contain multiple dated tuff horizons. We use the 10.35 ± 0.06 Ma (Ulloma tuff), 9.03 ± 0.07 Ma (Callapa tuff), and 5.35 ± 0.003 Ma (Toba 76 tuff) $^{40}Ar/^{39}Ar$ ages of sanidine (Marshall et al., 1992) associated with the stratigraphic section of Garzione et al. (2006) (Figure 1, labeled U 10.35, Cal 9.03, and T 5.35). Additional information regarding geochronology and thermochronometry samples is provided in the supporting information (Tables SI 1–SI 3).

Initial deposition in the Beni basin and the SAZ is inferred to be 27–30 Ma based on vertebrate and leaf fossils in the basal, conglomeratic Bala Formation (Baby et al., 1995). Thick sedimentary accumulations in SAZ synclines range from 4 to 7 km thick with lower units composed of FB deposits overlain by interbedded conglomerates from increasingly proximal thrust faults (Baby et al., 1995; Rodriguez & Fernando, 2002). Laser total-fusion $^{40}Ar/^{39}Ar$ ages from sanidine collected from an interbedded tuff produced a geochronology age of 22.1 ± 0.18 Ma (Mosolf et al., 2011). The sample was collected from the western limb of the Beni Syncline and is located between the axis of the syncline and the contact between Tertiary and Paleozoic rocks (Figure 1, label B 22.1).

2.4. Wedge-Top Formations

Wedge-top sediments, deposited on deformed and eroded Paleozoic rocks in the EC constrain the timing of deformation in the FTB. The Oligocene Salla Formation is located just south of the Beni cross section in the EC backthrust belt (Leier et al., 2010; McFadden et al., 1985; McRae, 1990) (Figures 1 and 2). Three interbedded tuff samples form the Salla Formation were dated: two using $^{40}Ar/^{39}Ar$ step heating of biotite and produced ages of 28 ± 0.68 Ma and 24.59 ± 0.39 Ma (Gillis et al., 2006) and one using biotite K/Ar mass spectrometry produced an age of 26.4 ± 1.0 (Figure 1, labeled S; MacFadden et al., 1985; Kay et al., 1998). The gently deformed Salla Formation was deposited from 29 to 24 Ma, with youngest detrital-zircon U-Pb ages of 28.3 ± 0.6 Ma, from strata immediately below the Salla formation in the Luribay Conglomerate, a coarse synorogenic conglomerate deposited unconformably above deformed and eroded Devonian and Silurian strata (Leier et al., 2010). Subcrop maps of the Paleozoic section underlying the Salla Formation and Luribay conglomerates suggest 4.5–6 km of material was removed prior to deposition (Leier et al., 2013). The Peñas and Aranjuez Formations (sanidine laser total-fusion ages of 27.41 ± 0.06–25.29 ± 0.04 Ma) are also in unconformable contact with deformed Devonian rocks in the EC backthrust belt and are located northwest

and southeast of La Paz, respectively (Figure 1, labels P and A) (Murray et al., 2010). The unconformable contact beneath the Oligocene units requires both deformation and erosion in this region of the EC backthrust belt prior to their deposition. The late Miocene Cangalli Formation, located in the eastern EC forethrust zone, unconformably overlies Ordovician strata near the town of Mapiri (Mosolf et al., 2011) (Figures 1 and 2). Three interbedded tuff deposits, yielding individual sanidine laser total-fusion $^{40}Ar/^{39}Ar$ ages of 9.12 ± 0.07 Ma, 7.59 ± 0.51, and 7.41 ± 0.52 Ma (Figure 1, label Ca) (Mosolf et al., 2011), were collected in conjunction with a measured section, indicating deposition of this wedge-top formation was underway by ~10 Ma (Mosolf et al., 2011). Similar to Silurian and Devonian units in the backthrust belt, deformation and erosion of the Ordovician strata beneath the Cangalli Formation in the forethrust belt must predate its deposition.

2.5. Regional Thermochronology

Previously published low-temperature thermochronometry samples from the northern Bolivia FTB record the cooling of rocks through different closure temperatures and have been interpreted to represent deformation-induced exhumation (Figure 1) (supporting information Figure SI 1 and Tables SI 1 and SI 2) (Barnes et al., 2006; Benjamin et al., 1987; Gillis et al., 2006; McQuarrie et al., 2008). Early AFT and ZFT work on the Triassic plutons in the EC backthrust belt, northeast of La Paz, record 5–15 Ma AFT ages and a cluster of 30–45 Ma ZFT ages (Benjamin et al., 1987). Additional data, including AFT, ZFT, and K-Fels $^{40}Ar/^{39}Ar$, revealed an onset of initial exhumation at 45–40 Ma with a deceleration in the rate of cooling from 25–11 Ma (Gillis et al., 2006). Young AFT ages (15–5 Ma) argue for rapid cooling from ~10 Ma to present (Barnes et al., 2012, 2006; Benjamin et al., 1987; Gillis et al., 2006; Safran et al., 2006). Integration of these cooling ages and systems with a balanced cross section suggests a significant deceleration in the rate of deformation occurred between 25 and ~15–8 Ma (McQuarrie et al., 2008). The young pulse of rapid exhumation (~10 Ma to present) has been linked to both active uplift in the EC, (Whipple & Gasparini, 2014) as well as enhanced orography due to the mountain range reaching a critical elevation that amplifies precipitation (Barnes et al., 2012). Active deformation in the SAZ is confirmed by young 6 ± 2 Ma exhumation recorded by apatite U-Th/He (AHe) (Lease et al., 2016).

3. Methods

The goals of this study are to (1) evaluate the time when deformation initiated in the EC (55, 50, 40, or 30 Ma); (2) examine permissible rates of deformation; that is, are there time periods such as 50–35 Ma, 35–25 Ma, or 10–5 Ma that deformation is notably faster? and (3) assess the validity of a published cross section by observing the relationship between basement geometry, predicted cooling ages, and basin formation and depth. In essence, we evaluate if a proposed cross-section geometry can reproduce the measured cooling ages in the region. Addressing these questions requires sequentially forward modeling the cross-section deformation while taking into account the flexural loading imparted by thrust faults, an estimation of how topography evolves with time, the associated magnitude of erosion (and flexural unloading), and the resulting magnitude and location of sedimentation. In the following section we present the methods, assumptions, and input parameters that are necessary to perform the kinematic and flexural modeling (section 3.1); the thermokinematic modeling (section 3.2); and our methods for comparing the modeled sedimentation location, magnitude, and age to measured stratigraphic sections (section 3.3).

3.1. Sequential Deformation and Isostasy

Depending on when deformation began in the EC, initial deposition of the westward derived Eocene Potoco Formation (Horton et al., 2001) could predate initiation of deformation in the EC (30 Ma), be concurrent with deformation in the EC (40 Ma), or have a significant period of sedimentation postdate the initiation of EC deformation (50 or 55 Ma). To obtain the initial conditions for the kinematic models that specifically focus on deformation east of the Altiplano, we used *Move* (Midland Valley) to model two initial condition scenarios, one in which 200 km of shortening in the proto-WC produced a 2–4.4 km sedimentary basin (Potoco Formation) in the proto-Altiplano, and one in which 100 km of shortening produced 470 m thick Paleocene to early Eocene foreland basin before deformation jumped eastward. These initial kinematic models are not thermally modeled and simply set up two potential early Cenozoic basins in the Altiplano. Initial isostatic and topographic parameters used for these steps are presented in the supporting information. Sequential deformation and isostatic modeling of the cross section was performed in *Move* using both initial Cenozoic basin geometries. The sections were deformed via the fault-parallel flow algorithm, flexural

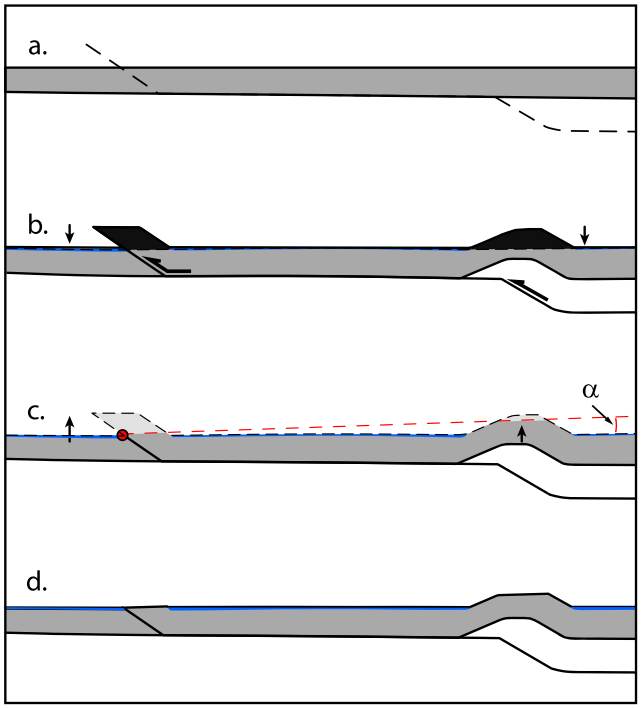

Figure 3. Illustration of deformation and isostatic compensation modeling sequence. Images show a (a) simplified restored cross section. (b) Motion on a fault (dashed line) and isostatic loading (black polygons) of material that is driven above the previous topographic surface by faulting. (c) Generation of new topography using critical wedge angle (α) that originates at the deformation front (red dot) and erosional unloading (grey polygons). (d) The new deformed, eroded cross section with predicted topographic surface and flexural basin (blue lines) is produced in each model step.

isostastatic loading (and unloading), and using the kinematics proposed by McQuarrie et al. (2008). A 0.5 × 0.5 km grid of unique points were displaced in ~10 km increments of shortening to produce vectors of displacement at each grid point that are converted to velocity fields by assigning time to each deformation step. After each ~10 km shortening step, the flexural isostatic load is calculated from the difference between the deformed topography and previously undeformed topographic surfaces (Figures 3a and 3b). The deformed and isostatically loaded topographic surface is used to estimate a new topographic surface by approximating topography as a westward increasing slope which initiates at the deformation front (point where the frontal thrust meets the surface; red dot, Figure 3c) (Dahlen, 1990). In the Bolivian Andes, this slope (α) has been shown to vary between 1 and 3° (Horton, 1999; Masek et al., 1994). Thus, the new calculated topography increases at an angle α where structural uplift has occurred and follows the previous topographic surface where it has not (Figures 3c and 3d). Basins are filled to 0 elevation and maximum elevation limits are applied when necessary in the EC, AP, and WC. Based on modern elevation maximums, elevations are limited to 6.5 km in the eastern EC, 5 km in the western EC, 4 km in the AP, and 6.5 in the WC. Therefore, topography in the eastern EC and eastern WC is reproduced by an average topographic slopes (α) of 1–3° (Horton, 1999; Masek et al., 1994) and 4° (Hoke & Garzione, 2008), respectively. Western facing slope angles are controlled by the footwall ramps and seldom exceed 15°. The maximum topographic angle on west facing slopes is limited to 45°, when structural rotation locally increases the modeled topographic slope. Material that lies above the new topographic surface (typically material above thrust ramps) is removed, and this erosion is isostatically balanced (light gray area; Figure 3c).

The dip of the modern décollement fault (indicated as β in critical wedge theory; e.g., Dahlen (1990) is a function of both the original sedimentary taper of the Paleozoic and Mesozoic strata (e.g., Boyer, 1995; Mitra, 1997) and the progressive load of the fold-and-thrust belt, which increases the dip of the décollement angle (β) through time (Stockmal et al., 2007; McQuarrie & Ehlers, 2015, 2017) (Figure 4). The 4° angle of the modern décollement is determined by seismic reflection, gravity, and well data (Watts et al., 1995; Baby et al., 1995; Zubieta Rossetti et al., 1996; Rodriguez & Fernando, 2002). Recreating this décollement dip and associated depth of the foreland basin occurs as the thrust load, calculated after each deformation step/increment, systematically depresses the grid in the foreland. Sedimentation is approximated by filling this basin to 0 km when the new topographic surface is estimated (Figures 3 and 4). By assigning an age to each kinematic step, the distance between paleosurface lines and their prescribed age becomes a predicted rate of deposition in the sedimentary basins that can be evaluated against measured data. Basins formed early in the model become incorporated into the FTB and erode, while the FB as a whole migrates toward the modern foreland. Basin accommodation is a function of the location of ramps (which facilitate structural uplift and isostatic loading), topographic height, the density of material, and the effective elastic thickness (EET) of the lithosphere. The final kinematic model reproduced the foreland and hinterland basin thickness, angle of the decollement in the foreland, and the modern geology and the topography along the line of section.

Multiple iterations of the flexural model were conducted to evaluate the parameters needed to most accurately reproduce the exposed surface geology, the depth of the FB, and the dip of the modern decollement by adjusting crustal density and EET in each iteration. During the emplacement of the first basement thrust sheet, EET was kept low (30 km) to preserve Ordovician units exposed at the surface, but systematically increased throughout the model (up to 90 km) to enhance the amount of sediment accumulation in flexural basins. Flexural models were performed with and without accounting for an additional sediment load

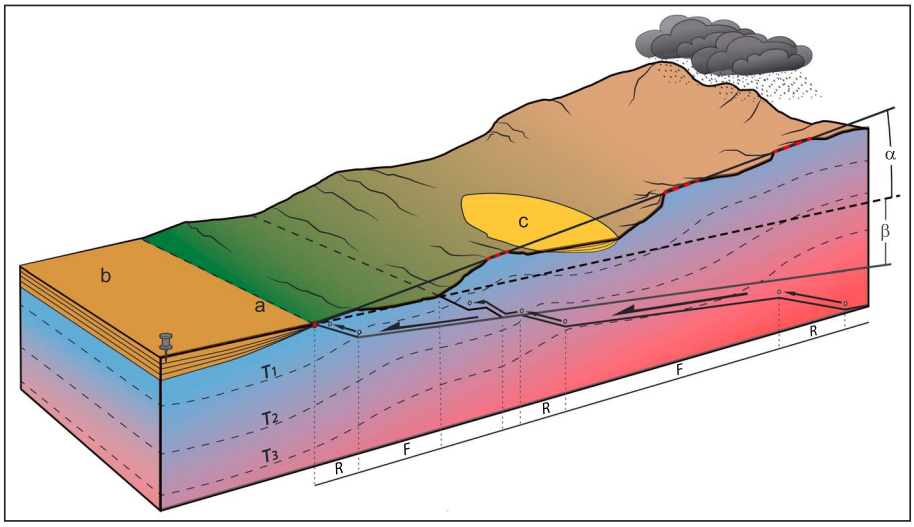

Figure 4. Box diagram describing modeled geologic processes in the FTB-FB system. Topographic surface is defined by a modified critical wedge theory with angle α originating at the deformation front (a) and defining the area above which erosion occurs, and angle β defined by the angle of the décollement flat. Sediment is accumulated in the FB (b) through isostatic loading and wedge-top sediment accumulation upon eroded surfaces (c). The model is pinned in the foreland allowing temporal evolution of the décollement through changing ramp locations and increasing décollement dip (β) by isostatic adjustments of thrust load. The location of ramps (R) and flats (F) strongly impact the timing of exhumation and thermochronometer cooling in Pecube. Subsurface material motion in the system deflects isotherms (dashed lines; T_1, T_2, and T_3) in the model relative to the rate of deformation.

for each increment of basin created. The upper limit of permissible loads was determined by loads that produced too little erosion (the correct geology is not exposed at the surface at the end of model) or sedimentation (topography of FTB is below SL) across the FTB. Because the flexural solution is nonunique, models that only accounted for thrust loads were able to approximate those with additional sediment loads by using higher thrust load densities (2900 kg/km^3) and EET (90 km) to lengthen the load distribution (Figure 5). Accounting for sediment loads modestly increased the depth (160–230 m) and width (~10 km) of the foreland basin (see supporting information section S2). Regardless of the load combinations, final simulations produced SAZ synclines that were 2 km too shallow and significantly lower topography ($>$ 3 km) in the EC and AP than modern topography.

To match the measured sedimentary basin depth and modern topographic height an imposed, long-wavelength uplift and subsidence (dynamic load) was applied to the EC and FB, respectively, to facilitate thick FB deposits and the high topography in the EC and AP. Adjustments were made incrementally at each 10 km step during the latter portion of the restoration, with the inflection point (between subsidence and uplift) located at the top of the modern ramp. Total magnitudes ranged from $-$3.3 km in the FB to 5.5 km in the hinterland (Figure S2). Geodynamic arguments in support of both dynamic subsidence of the FB and non-flexurally derived uplift/support for the Andean plateau are robust (Catuneanu, 2004; DeCelles, 2012; Eichelberger & McQuarrie, 2015; Garzione et al., 2006; Gurnis, 1993; Isacks, 1988; Lamb, 2011; Mitrovica et al., 1989; Ramos & Folguera, 2009) and elaborated on in section 5. However, the initiation of dynamic subsidence and uplift is unconstrained. We test the sensitivity of our results to when dynamic subsidence is initiated in two models. In the late subsidence (LS) model, dynamic adjustments initiate in conjunction with motion on basement sheet B. The timing of initiation of dynamic subsidence in the LS model ranges from 19.6 to 8 Ma depending on the velocity models tested, with the majority of simulations initiating LS between 19.6 and 12 Ma. In the early subsidence (ES) model, dynamic adjustments begin earlier, preceding a period of late Oligocene magmatism along the axis of the EC (Gillis et al., 2006; Sandeman et al., 1995). This time period has been interpreted as a shift from shallow to normal slab subduction (James & Sacks, 1999; Ramos & Folguera, 2009), coincident with the last stages of shortening in the EC-backthrust belt. Dynamic subsidence initiation ranges from 31.5 to 16.6 Ma for the ES model, with most of the models initiating ES between 31.5 and 25.6 Ma.

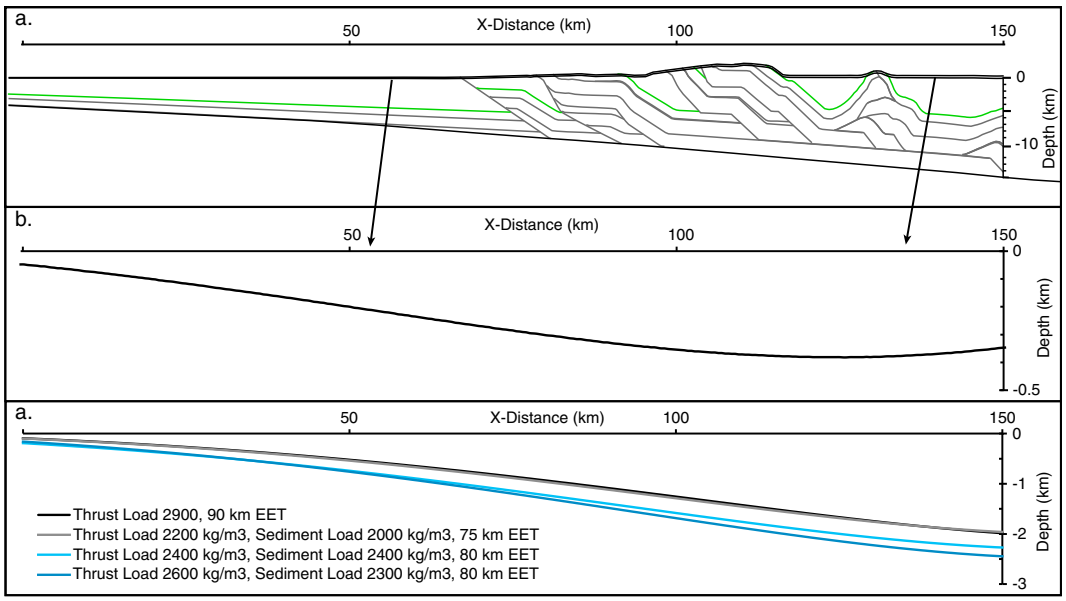

Figure 5. (a) Flexural loads produced by applying a load of 2,900 kg/m^3 to the rocks in the thrust belt with an EET of 90 km (lower topography line) when compared to applying a load of 2,600 kg/m^3 to the rocks in the thrust belt and a load of 2,300 kg/m^3 to the accumulated sediment in the produced basins with an EET of 80 km (Figure 5a; upper topography line). (b) The difference in sediment produced over the deformation in the model is a maximum of 400 m near the deformation front and thins with increasing distance. (c) Results from multiple tests of thrust and sediment loads and EET show the differences in accumulated sediment thicknesses in the modeled foreland basin.

3.2. Thermokinematic and Erosion Modeling

Displacement vectors and surface topographies from the kinematic model were input into a modified version of the thermal-kinematic and erosion model *Pecube* (Braun, 2003, 2005; McQuarrie & Ehlers, 2015; Whipp et al., 2009). The modified version of Pecube simulates the evolving subsurface thermal field based on input thermal parameters and the velocity fields determined from the sequentially deformed cross section (section 3.1) to derive the time-temperature (*t-T*) history of exhumed rocks based on their transport path (Figure 4). Predicted cooling ages of mineral systems along the model surface use thermochronometer kinetics described in Ehlers et al., (2005).

The 2-D model extends 900 km and represents the South American margin, after 100–200 km of shortening in the proto-Western Cordillera. It includes >80 km of length on the eastern and western edge to assure that the zero flux thermal boundary condition on the sides of the model does not influence thermal gradients near sample locations. The model extends to a depth of 110 km and maintains constant temperature boundaries at the surface and 1300°C at its base. Temperatures at the surface at sea level are 23°C (Santa Cruz yearly average, Deutscher Wetterdient (1991) and decreases with elevation at a rate of 5.3°C/km, the mean lapse rate measured in Bolivia (Gonfiantini et al., 2001). Radiogenic heat production (Ao) was varied from 0.5 to 1.0 μW/m^3. Values modeled for thermal conductivity and the specific heat capacity were 2.5 W/m K and 800 J/kg°K, respectively, in accordance with global averages of crustal rocks (Ehlers, 2005). All model parameters are summarized in Table 1 and expanded on in the supporting information. We evaluated the original geometric model proposed by McQuarrie et al. (2008) and a second, modified geometry including both the ES and LS dynamic subsidence models. All model results show that sedimentation in the foreland imparts a downward advection of the isotherms due to the deposition of sediments at surface temperatures that are then buried (e.g., Husson & Moretti, 2002), and isotherms that are advected upward by thrust faults, ramps, and associated erosion (e.g., Lock & Willett, 2008; Rahn & Grasemann, 1999; Shi & Wang, 1987) (Figure 4).

We compare the predicted ages to published ages to identify the range of velocity histories that reproduced the observed thermochronometer ages along the structural cross section. Specific groups of thermochronometers were omitted from the comparison including samples with ages older than the initiation of model (>55 Ma), AFT samples associated with Tertiary plutonism in the central EC, and two samples along the Rio

Table 1
Pecube Thermokinematic Modeling Properties

	Input values	Reference
	Material properties	
Crustal volumetric heat production	0.5–1.0 mW/m^3	Lucassen et al. (2001), Ehlers (2005), Springer (1999), Babeyko and Sobolev (2005), and Tassara (2005)
e-folding depth	None	
Thermal conductivity	2.5 W/m K	Lucassen et al. (2001), Ehlers (2005), Hamza et al. (2005), Springer (1999), Babeyko and Sobolev (2005), Arndt et al. (1997), and Tassara (2005)
Specific heat	800 J/kg K	Ehlers (2005), Springer (1999), Babeyko and Sobolev (2005), and Arndt et al. (1997)
	Numerical properties	
Model base	110 km	McQuarrie and Ehlers (2015)
Temperature at base	1300°C	McQuarrie and Ehlers (2015)
Temperature at surface	0 km 23°	Deutscher Wetterdient (1991)
Atmospheric lapse rate	5.3°/km	Gonfiantini et al. (2001)
Kinematic grid spacing	0.5 km	
Displacement increment	~10 km	
Model domain	900 × 110 × 5 km	
Horizontal node spacing (numerical model)	0.5 km	
Vertical node spacing (numerical model)	1.0 km	
Model start time	100 Ma	

La Paz river associated with recent incision (supporting information section S6 and Tables SI 1–SI 3). Velocity models ability to intersect published thermochronometers (within their errors) for three models (ES-0.7 Ao, ES-0.6 Ao, and LS-0.6 Ao) is used as a metric to compare models independent of initiation of dynamic subsidence and Ao. The range of fits determined by the thermochronometric modeling is combined with the chronostratigraphy model fit (section 3.3) to attain a total goodness of fit metric for each velocity model (section 4.5).

3.3. Basin Chronostratigraphic Constraints Used

When new topography is generated in the kinematic model, the FB elevation, as well as the Altiplano Basin elevation, is set to 0 km. The Altiplano basin forms at sea level until deformation initiates in the region. To continue sedimentation with deformation in the Altiplano, sediment is preserved in topographic lows up to the level of the bounding ranges or a maximum of 1 km during each deformation step.

As the isostatic load is accounted for, the previous elevation horizon, which represents the depositional surface of the basins at that time, subsides creating a modeled stratigraphy. These modeled stratigraphic ages, as determined by the applied velocity model, were compared to published chronostratigraphy to determine temporal relationships between modeled thermochronometer cooling and sediment accumulation (Figure 6). The stratigraphic location of dated ashfall beds in the hinterland and foreland (section 2.2) was compared to modeled sediment ages in each of the velocity models. Samples were placed in the stratigraphic column by using their mapped locations and orientations (Figure 2). Uncertainty related to assigning the map location of the sample into a projected stratigraphic section results in a sample placement error of ±500 m and is further discussed in supporting information section S5. The error in sample locations correlates to a 1 km thick package of modeled stratigraphy, which has different age estimates for the upper and lower bounds depending on the model velocities (Figure 6).

The timing of wedge-top sediment deposition (section 2.3) was determined by assuming deposition must occur after deformation and erosion have initiated, but before deformation has totally ceased in the area. The lower age limit is set by the magnitude of shortening needed to deform and erode Paleozoic formations to the level of exposed strata preserved immediately below the wedge-top formations (up to 5–7 km erosion see Leier et al., 2010, 2013). Upper bounds are set by the magnitude of shortening needed to produce proximal deformation that could cause structural damming, facilitate deposition, and impart the modest deformation observed in the preserved strata (Leier et al., 2010; Mosolf et al., 2011). It is assumed that localized downslope deformation could cause structural barriers, facilitating ponding and sediment accumulation

(Leier et al., 2010; Mosolf et al., 2011). Velocity models are described as matching the wedge-top sediment data if geochronology samples fall between deformation-induced erosion of the unit below the wedge-top formation and prior to the cessation of local deformation in the area. Erosion of local fault induced uplifts provided the sediment source for deposition (Leier et al., 2010). While wedge-top sediments are not specifically reproduced in the modeling process, the time windows in which they may be deposited are defined by the velocity model applied (Figure 6).

4. Results

4.1. Sequential Deformation and Evolving Cooling Ages

The initial kinematic model is based on the geometry and kinematics proposed by McQuarrie et al. (2008). To illustrate the effect of geometry on the predicted cooling ages, we examine the evolution of the FTB and the predicted cooling ages through time. Although the kinematic model reproduces the geometry and pattern of deformation of the cross section (compare Figures 2 and 8a), the algorithms used by *Move* to deform the section prevent a perfect match between the original and modeled sections. Because of this, the initial kinematic model has 8 km less shortening (268 km) than the McQuarrie et al., 2008 section (276 km). For the initial model we apply a constant velocity model with the start of deformation at 50 Ma so that initiation of deformation predates the oldest cooling ages measured in the EC (Benjamin et al., 1987; Eichelberger et al., 2013; Gillis et al., 2006). The 268 km of shortening over 50 Myr provides a shortening rate of 5.36 mm/yr. At 45 Ma, the emplacement of basement thrust sheet A (Figure 7) focused exhumation above the footwall and hanging wall basement ramps and reset thermochronometers. The initial modeled U-shaped cooling patterns above basement ramps (after 26 km of shortening) (Figure 7b, 45 Ma) display age patterns that are the youngest at the top of the basement footwall ramp and show a gentle increase in age toward the tip of the hanging wall ramp before the steep increase in ages that represent a suite of partially reset to nonreset ages. As basement sheet A continues to be emplaced, two U-shaped patterns in ages develop as a result of motion of material over the footwall ramp in the west and the hanging wall ramp in the east (Figures 7c and 7d). The shape of these curves is a function of the distribution of unreset (prestart of model), partially reset (the steep limbs of the U-shape), and reset cooling ages (Lock & Willett, 2008; McQuarrie & Ehlers, 2017). Thus, the oldest fully reset ages (indicating age and location of initial thrusting) are centered on the EC and young toward the west and east (Figure 7e, 25 Ma). Sediment accumulation in flexural basins to the east and the west of the basement thrust fault preceded (in time) the deposition of rocks currently preserved in the Beni FB (east) and Altiplano basin (west). These early basin sediments are eroded and redeposited farther away from the initial locus of deformation in the EC. Isostatic loading of the model depressed the modeled grid in the FB with respect to the topographic surface, imparting sequentially cooler thermal histories to these points. The activation of thrust sheet B focused exhumation above the new basement ramp (160–180 km) and in select SAZ thrust sheets in front of the basement thrust sheet (Figure 7f, 14 Ma). The emplacement of the basement sheet B resets lower temperature AFT and AHe systems above its footwall ramp, which moves west relative to the pinned FB (Figure 7g, 5 Ma). Synclinal basins fill as isolated fault sheets reach the erosional surface in the SAZ. At the final model step (Figure 7h, time 0), low-temperature AFT and AHe systems are variably reset in the SAZ thrust sheets and display a younging trend from the IAZ to the active ramp under the EC. The predicted cooling spectra display the oldest reset ages in the center of the EC and younger ages to both the east and west producing a prominent triangle pattern of reset ages. The pattern is a direct consequence of motion of rocks over the large (~10 km) hanging wall and footwall ramps of basement thrust sheet A. The young AFT and AHe predicted cooling signatures in the eastern EC increase in age toward the IAZ and are the result of material moving over the footwall ramp associated with basement sheet B. The youngest reset AFT and AHe ages in the SAZ are located at the base of thrust sheets that have been significantly eroded.

The youngest predicted AFT ages in the EC are not colocated with the young AFT measured ages in that region (Figure 7i). The predicted young AFT ages are $>$10 km to the east, associated with active uplift occurring over the SAZ basement ramp. The colocation of the ramp and youngest predicted ages strongly suggest that the active ramp is located west of its interpreted location for the measured ages to match the predicted ages. The simplest way to move the footwall ramp farther west than where it was initially proposed by McQuarrie et al. (2008) is by increasing shortening in the SAZ and thereby increasing the displacement over the ramp. A modified kinematic scenario was developed to account for increased shortening in the SAZ and IAZ that still matches the geological relationships preserved at the surface. The increased shortening in the

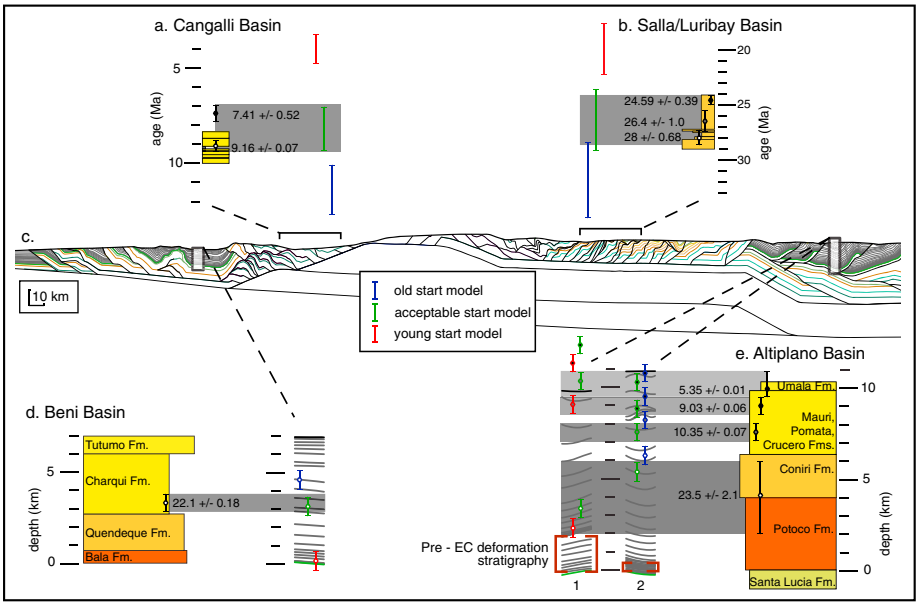

Figure 6. Basin sediment correlation diagram showing uncertainty envelopes associated with each sample. The four sedimentary basins (a) Cangalli and (b) Salla/Luribay, (d) Beni, and (e) Atiplano described in Figure 2 are shown with respect to their (c) position in the FTB. Wedge top basins (a) Cangalli and (b) Salla/Luribay are plotted above the cross section with age on the vertical axis. Published geochronologic ages of wedge-top formations are plotted with age error bars in a simplified stratigraphic column. Colored bars extend across permissible wedge-top deposition windows between age of Paleozoic formation erosion and age of localized deformation (providing sediment dams) modeled deposition initiation, and completion. Bars are shown as (1) acceptable start model (green), (2) a model that is too old (blue), and (3) a model that is too young (red). Gray bands highlight acceptable windows between the end of erosion and the end of wedge-top deposition. Modeled bars that plot outside of grey bands are considered an unacceptable fit. Foreland and hinterland basins, (d) Beni and (e) Atiplano, are plotted below the cross section with depth (in km) on the vertical axis. Published geochronologic ages are shown with the error bars (±500 m), associated with each basin sample location in a simplified stratigraphic column. The modeled stratigraphic columns are plotted adjacent to the simplified stratigraphic section. The two modeled stratigraphic columns left of the Altiplano section represent (1) deposition of the Potoco Formation that preceded deformation in the EC and (2) deposition of the Potoco Formation that was concurrent with EC deformation. The bar and ball symbols on the modeled stratigraphic sections represent the depth at which that sample (geochronologic measured age) would plot in the modeled chronostratigraphy. Acceptable start models (green) plot within the grey bands highlighting a permissible depth range. An early model start (blue) places the modeled ball and bar symbols high in the stratigraphic section, while a model start that is later (red) places the symbol low in the stratigraphic section. Note that for Altiplano samples, early start ages are plotted only on the graph with minimal (<0.5 km) predeformational Potoco Formation and late start ages are plotted on the graph with 2–4 km of predeformational Potoco Formation.

SAZ facilitated the westward movement of the decollement ramp to match thermochronometer cooling data in the EC (Figure 8).

4.2. Revised Geometry and Imposed Subsidence

The geometry and the resulting kinematics proposed by McQuarrie et al. (2008) were altered to enable the westward shift of the basement decollement ramp. Westward movement of the active basement ramp was facilitated by both increasing SAZ shortening and increasing the total amount of displacement on basement thrust B. Increased slip must be distributed to SAZ thrust sheets that do not have preserved hanging wall ramps, allowing for additional fault motion at these locations. Revised total shortening along the balanced cross section is 285 km, 9 km more than the McQuarrie et al. (2008) section, but 17 km more than the initial kinematic model (SI Figure S4). The kinematics and associated erosional exhumation are similar to those described in the sequential deformation section (section 4.1) with the exception of an increase in exhumation in the eastern EC and on select SAZ thrust sheets. The increased shortening causes additional material to move over the active ramp in the EC and extends the young predicted AFT trend farther west (Figure 8). In addition, the increased shortening in the SAZ causes younger predicted AHe ages in that region. Modeling of central Andean orocline rotation also suggests an increase in SAZ shortening (~20 km) in northern Bolivia due

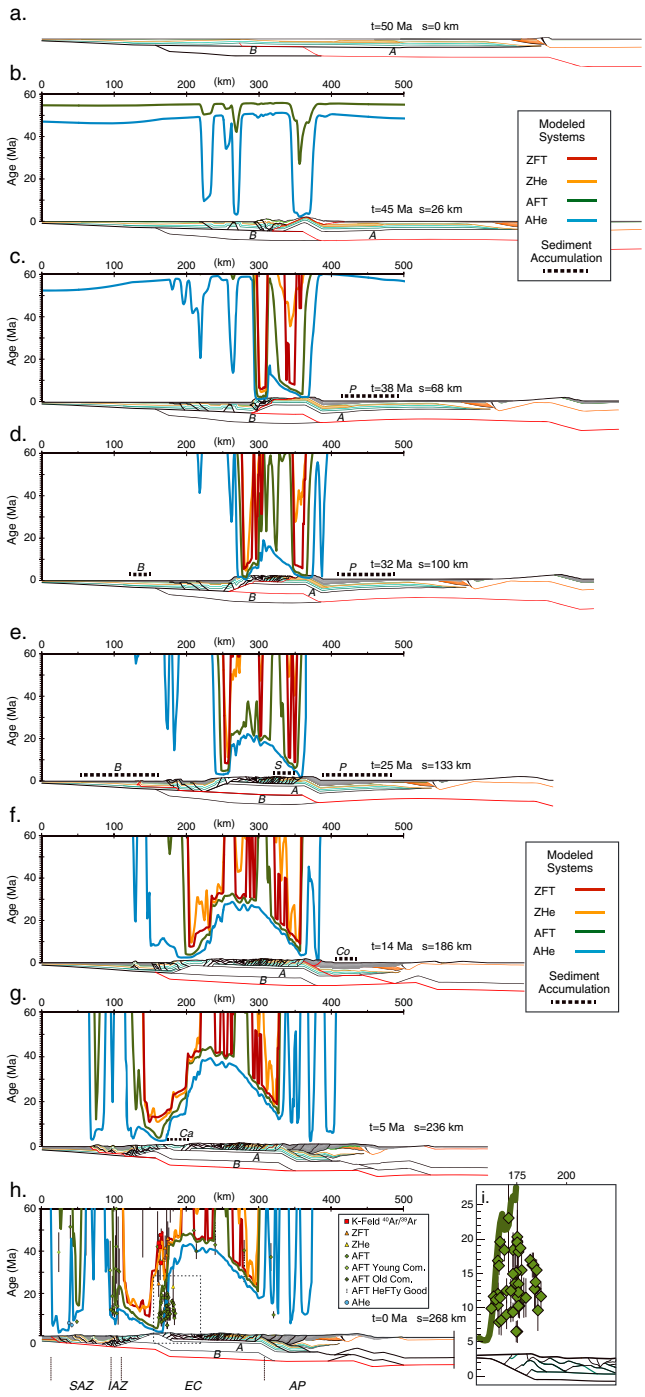

Figure 7. Structural and thermochronometric evolution diagram for of the northern Bolivian FTB using kinematic scenario 1 (McQuarrie et al., 2008). Sequential set of cross sections colored by formation age (Figure 1) and cooling signatures predicted from the Pecube model surface at each interval. The (a) restored cross section is (b–h) sequentially deformed with each panel displaying the geometry of the deformed model, prediction of thermochronometer cooling signatures, time (*t*), and amount of shortening (*s*). Sedimentation is denoted by a black dashed line; erosion of Paleozoic formations occur after the previous time step but before time of basin shown. Sediment accumulation is denoted by letter representing basin or formation name: Potoco (P), Beni Basin (B), Salla (S), Coniri (Co), and Cangalli (Ca). (h) AFT cooling ages are separated into young component cooling ages (AFT Young Comp.), old component ages (AFT Old Comp.), HeFTy modeled good match to the initiation of rapid cooling (AFT HeFTy Good; from Barnes et al., 2012), and pooled ages (AFT). (i) An enlarged plot of the EC AFT data and the predicted cooling signature.

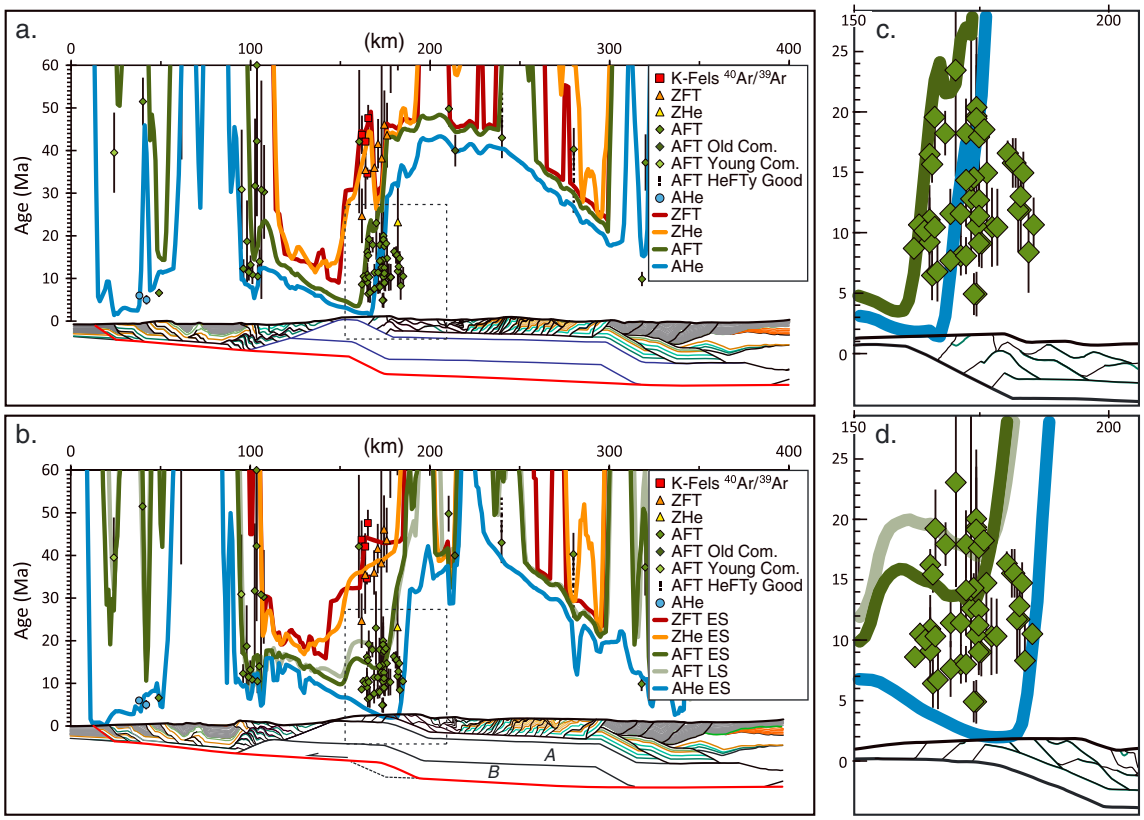

Figure 8. Predicted thermochronometer cooling spectra (a) for model that utilized kinematics from McQuarrie et al. (2008) and (b) for the modified kinematic model with increased shortening in the SAZ and IAZ ES model spectra and LS model AFT cooling signature. (c and d) Close-up of the central EC AFT and AHe predicted cooling trends. Difference in cooling trends at 150–200 km is related to increased motion of material up the footwall ramp (dashed line; Figure 8b).

to vertical axis rotation that is similar to the increase in shortening needed to fit the EC thermochronometer trends in this study (Eichelberger & McQuarrie, 2015).

We also applied vertical adjustments based on dynamic subsidence and uplift to the revised kinematic model. Both the LS and ES models produce the same total exhumation; however, the age of that exhumation differs. In the LS model, exhumation in the EC initiates earlier, predicting AFT ages that are ~5 Myr older in the central EC (150–180 km, Figures 8c and 8d) than the predicted ages from the more recent ES exhumation. Evaluation of the effects of age of deformation, velocity, and thermal parameters on cooling ages in the following sections utilize the ES and LS revised kinematic models for thermokinematic modeling.

4.3. Effects of Radiogenic Heat Production on Cooling Ages

Using a constant velocity model initiating at 50 Ma, a range of thermal parameters were used to investigate the sensitivity of the model to different thermal states of the crust. Reported Ao values for the upper crust in the Andes range from 0.85 to 1.30 $\mu W/m^3$ with lower crustal measurements and modeled estimates that range from 0.3 to 0.85 $\mu W/m^3$ (Babeyko & Sobolev, 2005; Ehlers, 2005; Lucassen et al., 2001; Syracuse et al., 2010). In this study, crustal Ao values are varied from 0.5 to 1.0 $\mu W/m^3$ to identify the range in predicted thermochronometer cooling ages with different thermal states of the crust. All velocity models presented in sections 4.1 use Ao = 0.6 $\mu W/m^3$.

Six different Ao values (0.5–1.0 $\mu W/m^3$) are evaluated for the ES, 50 Ma start constant velocity model to evaluate the magnitude of change in modeled cooling ages with changes in Ao. Increased heat production values promote elevated thermal gradients and result in younger predicted thermochronometer cooling ages because sample points cool through their closure temperatures later in the model. To a first order, the predicted AFT ages show minimal variations due to changes in Ao. The notable exception is a younging of predicted AFT ages with increased radiogenic heat production in the SAZ at 10–50 km and the central EC

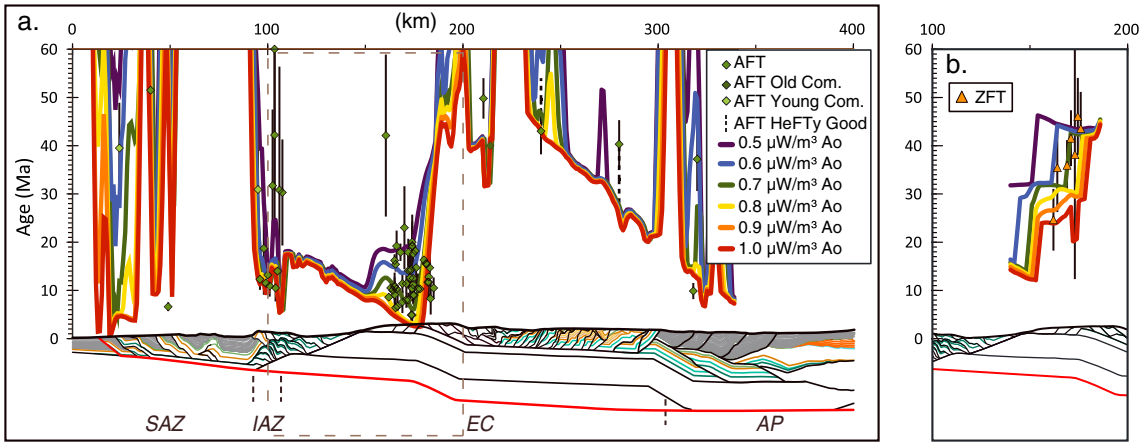

Figure 9. Predicted thermochronometer cooling spectra ((a) AFT and (b) ZFT) for the ES, constant velocity, and 50 Ma start model using different radiogenic heat production (Ao) values.

at 150–180 km (Figure 9a). Predicted AFT cooling ages are 15–17 Ma older for the 0.5 μW/m^3 than for the 1.0 μW/m^3 in the central-EC and 40–50 Ma older for samples in the SAZ (Figure 9a). Predicted ZFT ages show a similar degree of variability with changes in Ao. Predicted ZFT ages in the eastern EC (Figure 9b; 150–180 km) decreases by 15–20 Ma with increasing radiogenic heat production. For the constant velocity model, both predicted AFT and ZFT samples provide the best fit to observations when using Ao = 0.7, which is used as a preferred radiogenic heat production value.

4.4. Testing Deformation Age and Velocity

An optimal onset of deformation was determined by testing constant rate velocity models with different onset times for deformation (30–55 Ma) and comparing chronostratigraphy and predicted thermochronometer data sets. Rates of shortening increase with decreasing age of initiation, ranging from 5.2 to 9.5 mm/yr (grayscale lines Figure 10). Three different hiatus models (representing step functions in velocity), 25–15 Ma, 25–12 Ma, and 25–8 Ma, were tested to understand the chronologic constraints on post-15 Ma deformation in northern Bolivian Andes (McQuarrie et al., 2008). The hiatus models are based on the observed deceleration in the rate of cooling from 25 to 11 Ma within the EC (Gillis et al., 2006), synorogenic sedimentary rocks that limit EC deformation younger than 25 Ma (Gillis et al., 2006; Leier et al., 2010; Murray et al., 2010) and debate on the age of SAZ initiation (Garzione et al., 2008; Lease et al., 2016; McQuarrie et al., 2008; Oncken et al., 2006). These models partition significant SAZ deformation into decreasing windows of time, 15, 12, or 8 Ma, each with increased rates of shortening (violet and blue lines Figure 10). Two variable rate models, which resemble sine curves (green lines Figure 10), are presented to show more complex velocity model fits to the chronologic data, such as evaluating the upper and lower limits of permissible velocities and velocity change. These variable velocity models were tailored to match wedge-top constraints and ZFT trend in the EC. Each velocity model is evaluated based on the predicted thermochronometer cooling and match to geochronologic data, based on age and basin thickness (Figures 6 and 11).

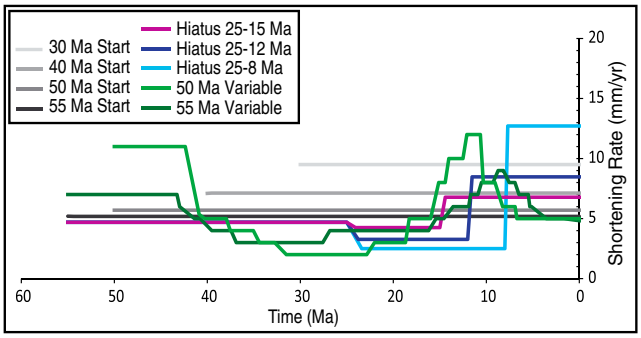

Figure 10. Velocity model plot illustrating the range of tested velocities. Constant velocity models (solid) exhibit an increase in rate with decreasing start date. Hiatus velocity models (dashed) display a decrease in rate at 25 Ma and an increase at 15, 12, or 8 Ma. Variable rate models resemble a sine curve with the 50 Ma model displaying greater amplitude variations in rate.

4.4.1. Fit of Velocity Models to Geochronology

The predicted age and depth of the modeled sedimentary basins can be compared to their measured equivalents (Figure 11). We compare the age and depth of dated strata from the Altiplano and Beni basins (Figures 1 and 2) to that predicted by the kinematic model, using a range of possible velocities. In addition, we compare the ages of the Salla and Cangalli wedge-top deposits (Figures 1 and 2) to that predicted by different velocity models. Published geochronologic ages of synorogenic strata are plotted with error bars that represent the

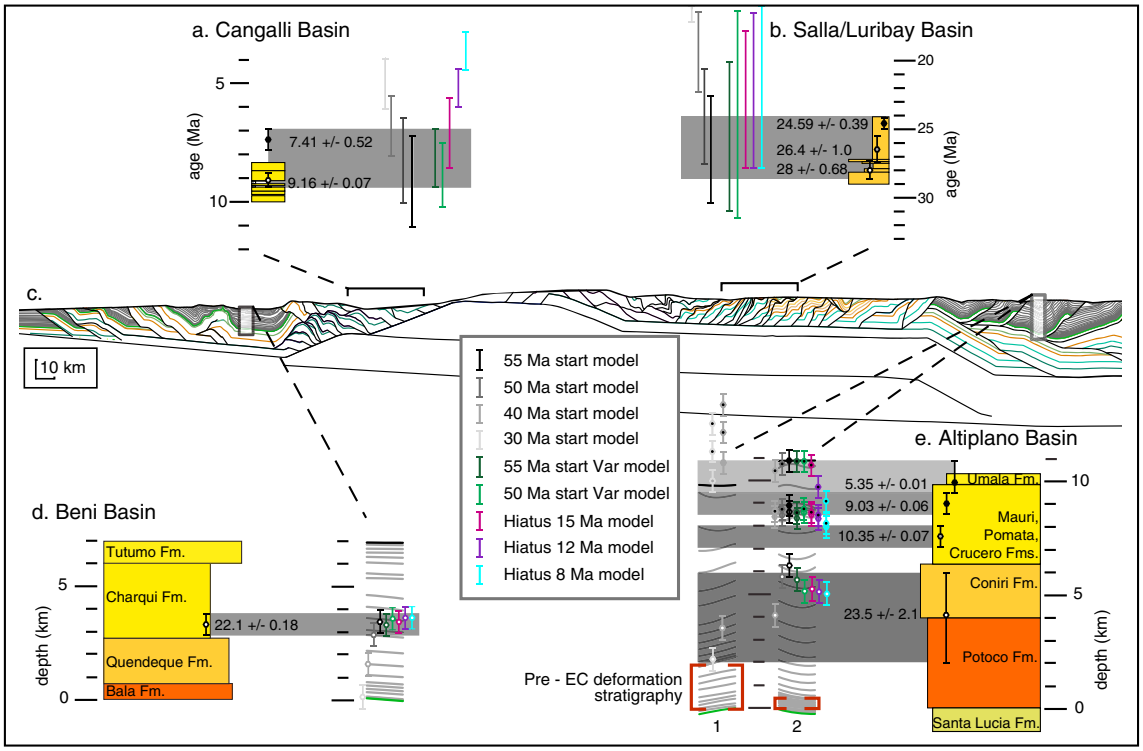

Figure 11. Modeled versus measured basin sediment correlation diagrams (see description in Figure 6). Grey bands extending across modeled wedge top basins (a) Cangalli and (b) Salla/Luribay highlight permissible wedge-top deposition windows between age of Paleozoic formation erosion and age of localized deformation with wedge-top deposition. If modeled bars (representing different start ages and deformation velocities) overlap with grey bands, then we interpret the modeled data to fit the published data. Grey bands extending across modeled foreland and hinterland basins (d) Beni and (e) Atiplano indicate permissible depth range for a given (measured) stratigraphic age. Bar and ball symbols highlight where measured geochronologic samples would plot in the modeled stratigraphy. If the modeled basin age is too young, then the bar and ball symbol would plot lower than the associated grey band. If the modeled age is too old, it will plot above the grey band. The two modeled stratigraphic columns left of the Altiplano section represent (1) deposition of the Potoco Formation that preceded deformation in the EC and (2) deposition of the Potoco Formation that was concurrent with EC deformation.

range in permissible depth (±500) in their measured sections (Figures 2 and 11). These ages are plotted again at their equivalent age in the modeled pseudostratographic sections. (Figure 11). Data points that are plotted higher in the pseudostratographic column than the equivalent data point location is in the measured stratigraphic column means that the age of basin formation (for that velocity model) is older than the measured age. If the data points are plotted lower in the pseudostratographic column, then the predicted basin is younger than the measured basin age. If the error bars overlap (between the measured and modeled sections), then we consider the modeled age an acceptable fit to the measured age. (Figures 2, 6, and 11). Models are described as matching wedge-top geochronology samples if the modeled ages, which bracket the time between erosion and structural damming, overlap the measured ages and associated error bars (Figures 2, 6, and 11). Bars representing constant velocity models with older start dates (50–55 Ma) intersect the error bars for both basin and wedge-top geochronology samples indicating the predicted age of the stratigraphy from the model matches the measured stratigraphic age. The 50 Ma start model intersects both basin samples but the 55 Ma start model predicts an AP basin age that is too old to match the measured 10.35 Ma age of the Ulloma tuff (Figure 11). Lines representing velocity models with younger start dates (40–30 Ma) exhibit decreasing fits to the geochronology samples, with the 30 Ma model predicting basin ages that are significantly younger than the measured ages except oldest AP basin sample (23.5 Ma) (Figure 11). The hiatus models diverge from the constant velocity models at 25 Ma and thus differ in their match to the Cangalli Formation samples and the younger AP samples. Models with older SAZ initiation (15 Ma) intersect young wedge-top sample ages; however, velocity models with a younger (12 and 8 Ma) SAZ start predict increasingly younger basin ages for both of the Cangalli Formation samples. Both the 50 and 55 Ma start variable velocity models were tailored to match early ZFT and AFT cooling ages in the EC, Oligocene wedge-top erosion and sedimentation windows in the western

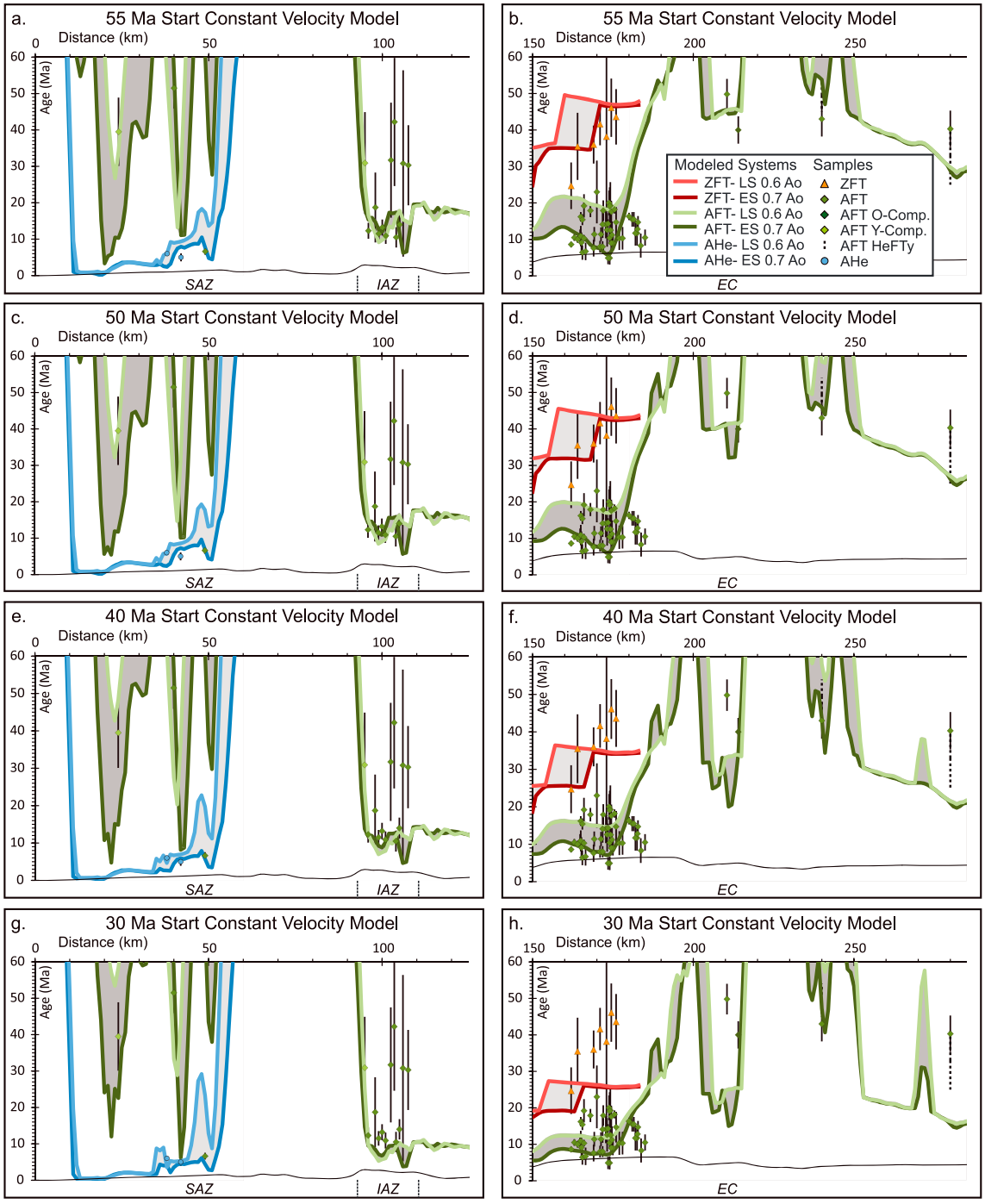

Figure 12. Predicted thermochronometer cooling plots for constant velocity models with different ages of initiation: (a, b) 55 Ma start, (c, d) 50 Ma start, (e, f) 40 Ma start, and (g, h) 30 Ma start.

EC, and AFT cooling and wedge-top erosional constraints in the IAZ and eastern EC. The two variable velocity models display a cyclic pattern in the rate of shortening to match theses geochronologic constraints.

4.4.2. Fit of Constant Velocity Models With Published Thermochronometer

Thermochronometer samples, with their error estimates, have been plotted along the structural cross section with dashed lines representing times of rapid cooling identified in HeFTy models (Barnes et al., 2012). These data are compared to predicted cooling signatures with a 1 km horizontal resolution (Figures 12–14). Predicted thermochronometer ages were three-point averaged and plotted using a 1 Ma thick line and

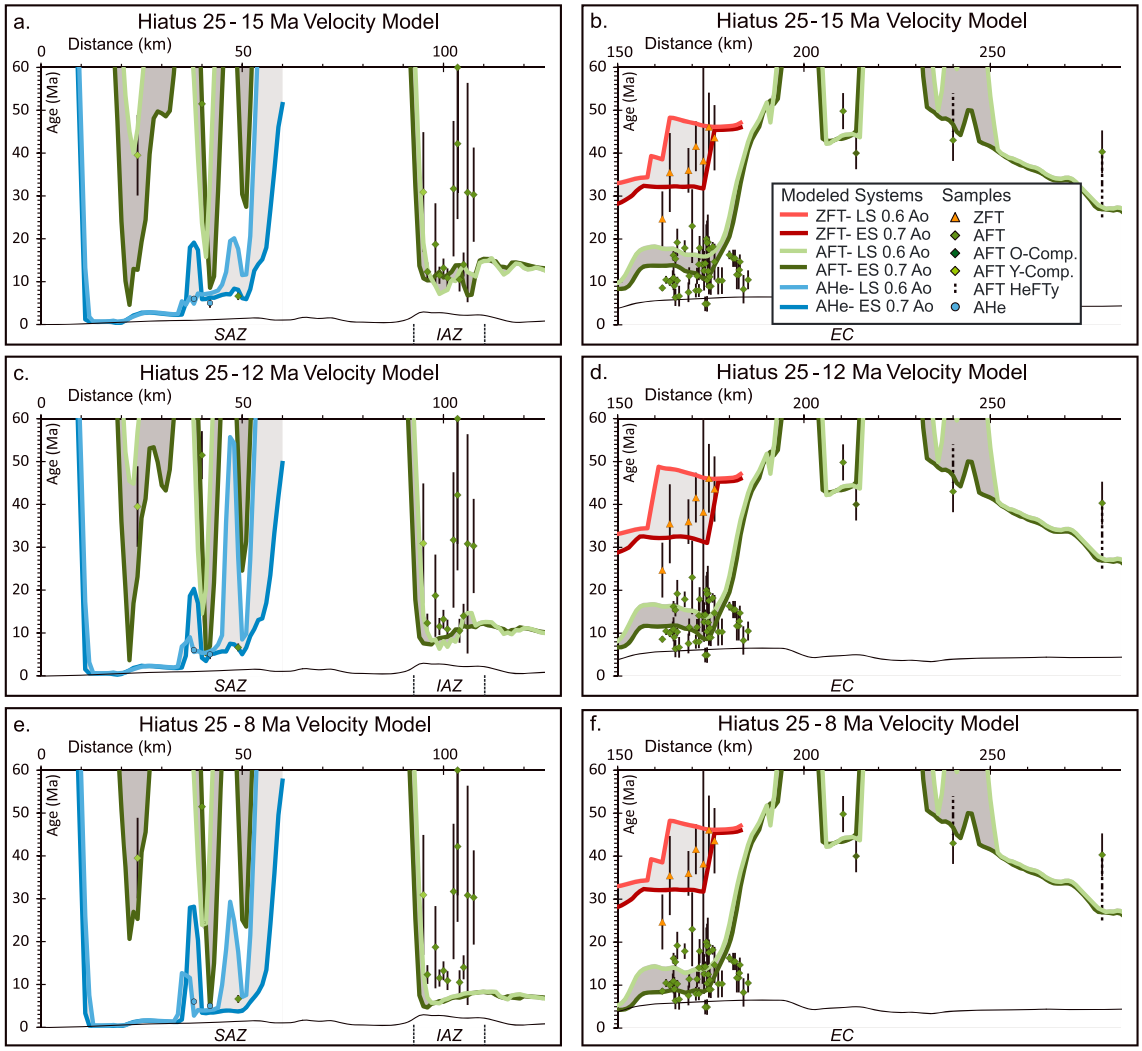

Figure 13. Predicted thermochronometer cooling plots for 55 Ma start hiatus models with different SAZ age of initiation:(a, b) 15 Ma SAZ initiation, (c, d) 12 Ma SAZ initiation, and (e, f) 8 Ma SAZ initiation.

illustrate the match between modeled cooling signatures, errors of samples and HeFTy modeled rapid cooling along the modeled cross section. Models are rated by their ability to intersect samples' errors and HeFTy modeled rapid cooling along the modeled section. We plot lines representing the results from both ES-0.7 Ao and LS-0.6 Ao models together to illustrate a window of acceptable predicted thermochronometer cooling ages for each velocity model. The ES model and higher Ao values both produce younger cooling ages, while the LS model and lower Ao values produce older ages. This method was employed to interrogate the effects of velocity on cooling ages while acknowledging the uncertainty related to Ao and the initiation of subsidence.

Constant velocity models display variation in predicted thermochronometer ages based on model initiation age (Figure 12). There is a decreased match with younger age start models with ZFT and AFT in the EC and AFT in the IAZ. The older age start constant velocity models (50–55 Ma) match six of the seven ZFT samples in the EC (Figures 12b and 12d). The 40 Ma start model matches five, and the 30 Ma start model only matches two of the ZFT samples in the EC (Figures 12g and 12h). Older start date (50–55 Ma) models predicted AFT cooling signatures for the EC backthrust belt (200–280 km Figures 12b and 12d) that intersect two of the four samples and both modeled HeFTy cooling windows. Younger start date models (30–40 Ma) also match two of the four AFT samples but only intersect one of the two HeFTy modeled cooling windows (Figures 12f and 12h). In the central EC (from150 to 190 km) all models predict cooling ages that match the

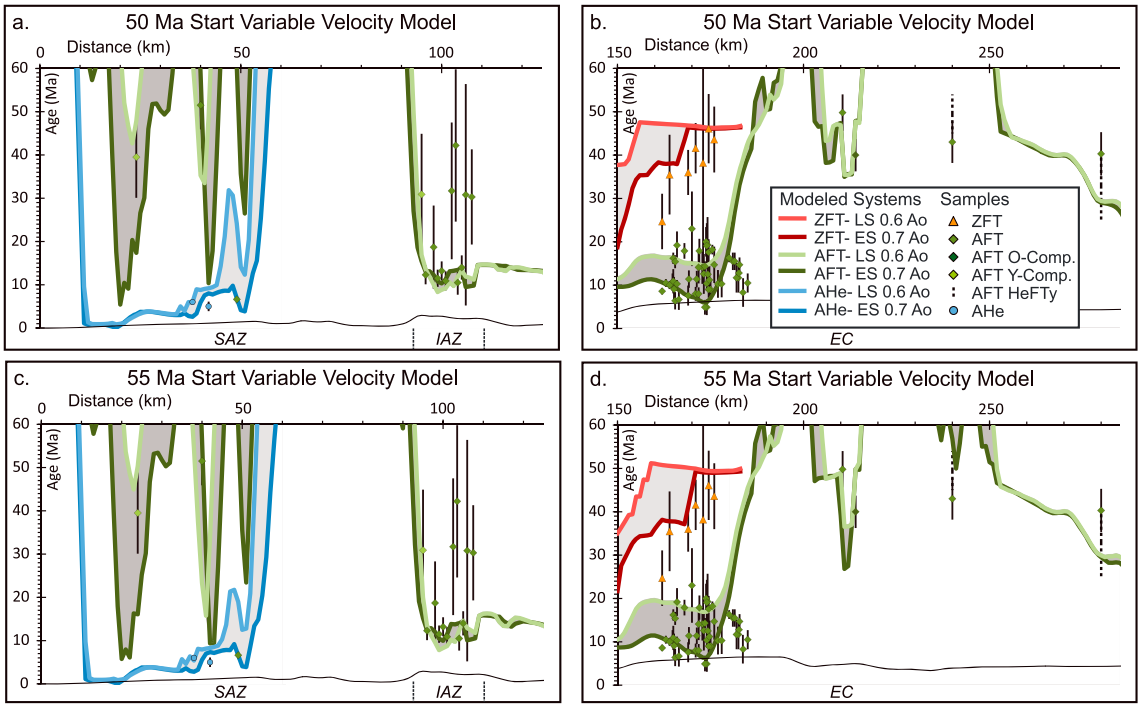

Figure 14. Predicted thermochronometer cooling plots for variable velocity models with different ages of initiation: (a, b) 50 Ma start variable velocity and (c, d) 55 Ma start variable velocity.

measured ages (Figures 12b, 12d, 12f, and 12h). The largest difference in predicted ages in this region is the wider range of predicted ages with the slower shortening rates. The older start models predict older AFT ages in the models with earlier exhumation (LS) and lower heat production values (Ao). The faster shortening rates due to younger start dates produce modeled ages that are much less sensitive to the dynamic subsidence model (LS or ES) or heat production values. Thus, the predictive window of cooling between the ES-0.7 Ao and LS-0.6 Ao models is much narrower (Figure 12). In the IAZ (from 90 to 110 km), the 50 and 55 Ma start models matched 10 of the 12 AFT samples, while the 40 and 30 Ma start models matched 8 and 7 of the 12 samples, respectively (Figures 12a, 12c, 12e, and 12g). The AFT cooling signals in the SAZ are indistinguishable and all produce matches to two of the three samples in all constant velocity models tested. The westernmost thrust sheet (50 km) does not match the measured AFT sample in any of the velocity models, suggesting that additional 1–2 km out-of-sequence thrusting may be necessary on this fault to account for this reset age. In the SAZ, models with younger start dates (40–30 Ma) match both of the AHe samples, while models with older start dates match only one of the two samples (Figures 12a, 12c, 12e, and 12g). As a whole, older initiation age constant velocity models have a greater match to thermochronometer cooling ages.

4.4.3. Fit of Variable Velocity Models With Published Thermochronometer Data

Hiatus velocity models show the differences in thermochronometer cooling signals that are controlled by the age of SAZ deformation (Figure 13). When comparing hiatus models, a slight increase in the match of thermochronometers (especially in the IAZ) is found with hiatus models with older (12 and 15 Ma) SAZ initiation. Because the hiatus models' velocities are the same from 55–25 Ma, older cooling signals (specifically in the EC) are identical (Figures 13b, 12d, and 12f). The models diverge in their predictive cooling signatures in the central EC, IAZ, and SAZ based on the initiation of the SAZ deformation (15, 12, and 8 Ma). The IAZ shows a clear decrease in fit as the SAZ initiation becomes younger and the predicted ages intersect less of the measured AFT samples (95–105 km; Figures 13a, 13c, and 13e). Surprisingly, our modeling showed no difference in the predicted AFT or AHe cooling signals in the SAZ between the hiatus models tested (Figures 13a, 13c, and 13e). Both variable velocity models tested result in nearly identical thermochronometer cooling signal fits (Figure 14). The variable velocity models differ in the EC with the 55 Ma start variable velocity model intersecting more of the ZFT and AFT in the EC (Figures 14b and 14d).

Table 2
Comparison of Model-Predicted Chronology to Thermochronometer and Geochronology Samples

	Thermochronometers						Synorogenic sediments						
	SAZ-AHe	SAZ-AFT	IAZ-AFT	EC-AFT	W-EC-AFT	EC-ZFT	Salla Formation	Cangalli Formation	SAZ	AP	Total		
	Total samples												
Location/type	2	3	12	47	4	7	3	2	1	4	85	Total % fit	Total % fit ES 0.7 Ao
						Constant velocity							
55 Ma	0–1	1–2	7–9	11–16	2–3	4–6	3	2	1	3	35–44	41–52%	52%
50 Ma	0–1	1–2	8–10	13–16	2–3	5–6	3	1	1	4	38–45	45–53%	53%
40 Ma	1–2	1–2	7–8	12–16	2	3	3	1	0	4	37–41	44–48%	46%
30 Ma	1–2	1–2	4–8	12–18	1–2	1–3	0	0	0	1	24–35	28–41%	33%
						Hiatus velocity							
Hiatus 25–15 Ma	1–2	0–2	7–8	12–16	2	4–5	3	1	1	4	38–43	45–51%	45%
Hiatus 25–12 Ma	1–2	1–2	4–5	13–15	1–2	4–5	3	0	1	4	34–36	40–42%	42%
Hiatus 25–8 Ma	1	2	0–4	14–18	2	4–6	3	0	1	4	35–36	41–42%	41%
						Variable velocity							
55 Ma variable	0–1	1–2	7–8	12–17	3	3–5	3	2	1	4	38–44	45–52%	52%
50 Ma variable	0–1	1–2	8–9	13–16	3	4–5	3	2	1	4	40–44	47–52%	52%

Note. Predicted thermochronometer ages are plotted with 1 Ma thick lines and must intersect age of sample or within its error or HeFTy onset of rapid cooling windows. Predicted ages of synorogenic sediment samples are also plotted with a 1 Ma thick line and must plot within the error of each sample. Range of thermochronometer values indicate matches for LS 0.6 Ao, ES 0.6 Ao, and ES 0.7 Ao modes. The total fit is attained by dividing numbers of chronometers that fit the model by the total chronometers along the modeled sections.

4.5. Best Fit Models

Velocity models were compared based on their ability to match the thermochronometry and geochronology data along the modeled section with equal weight given to each sample (Table 2). The total percent fit for each model was calculated by dividing the amount of chronologic samples intersected by the total samples along the modeled section. Matches were evaluated using both the models' ability to match the geochronologic ages (section 4.4.1) as well as the number of modeled thermochronometer ages that intersected measured cooling ages. Velocity model fits were evaluated using predicted thermochronometer cooling signatures from the ES kinematic model with Ao of 0.7 and 0.6, and the LS kinematic model with Ao of 0.6. These models define the boundaries of, and plot within, the window of acceptable fits determine through varying age of exhumation (ES and LS models) and radiogenic heat production (Figures 13–15). The range of fits to all three models are shown in Table 2. Older start times in the constant velocity models (55 Ma and 50 Ma models) have the best fits (41–52% and 45–53%; Table 2). Younger start constant velocity models (40 Ma and 30 Ma models) do not fit the data as well (44–48% and 28–41%; Table 2). The older SAZ initiation hiatus velocity model (Hiatus 15 Ma) has the best fit (45–51%; Table 2), with lower fits for models with a Hiatus at 12 Ma and at 8 Ma (40–42% and 41–42%; Table 2). Variable velocity models specifically match all of the geochronology data points and have fits of 45–52% (55 Ma variable) and 47–52% (50 Ma variable) (Table 2). The ES kinematic model with Ao of 0.7 has the highest percentage fit in nearly every velocity model tested (Table 2), except for the hiatus 25–15 Ma model where ES models with Ao of 0.6 intersects more of the older ages in the cluster of EC AFT samples (Figure 13b). The highest fit models tested were used to define a range of optimal velocity models. Models with fits of 50% or greater have been used to define an envelope of acceptable velocity of deformation for northern Bolivia. This fit was chosen because multiple models have matches of 50% or greater and there is a larger break in fit between 51% and the next best fit, 48%. The acceptable velocity envelope is composed of the variable and constant velocity models with 55 and 50 Ma start dates and the 15 Ma Hiatus velocity model (Figure 15). The envelope of acceptable deformation suggests

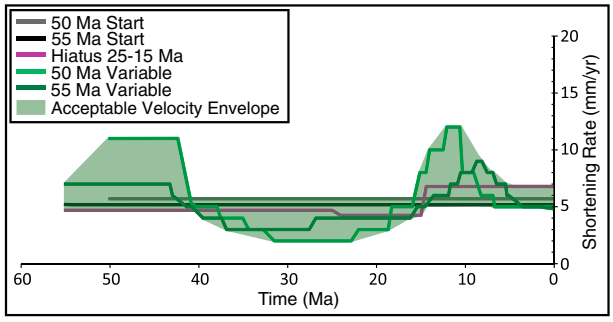

Figure 15. Shortening rate versus time graph showing envelope of acceptable rates of deformation for the northern Bolivia modeled cross section.

deformation may have occurred at a constant pace from 50–55 Ma or rapid shortening may have a periodicity of ~40 Ma separated by times of low shortening.

5. Discussion

5.1. Cooling Signals Imposed by Large Basement Thrust Sheets

Cooling ages in the Bolivian Andes to a first order reflect the emplacement of basement thrust sheets. In our model the location of basement ramps through time focuses uplift, producing high topography, causing concentrated erosion, exhumation, and thermochronometer cooling. The motion of material up the hinterland footwall ramp imparts the westward younging cooling signal recorded in EC backthrust belt samples (Figures 8a and 8b, 250–300 km). The eastward propagation of the basement (sheet A) hanging wall ramp forms a crustal-scale passive-roof duplex producing an eastward younging cooling pattern in the EC as material moves over this frontal hanging wall ramp (Figure 7h, 200–300 km). The combination of these basement ramps produces a triangular cooling pattern with the youngest predicted ages in the east and west that matches the measured thermochronometer ages across the EC (Figures 8a and 8b). The clustering of young ($<$15 Ma) AFT cooling ages in the central EC is a function of the active basement ramp, which is linked to shortening in the SAZ. Previous interpretations of this recent cooling expressed as young AFT ages include active deformation manifested as surface breaking faults or subsurface accretion (Norton & Schlunegger, 2011), focused erosion driven by an increase in precipitation (Barnes et al., 2012; Gillis et al., 2006; Lease & Ehlers, 2013), and uplift over a basement ramp (Whipple & Gasparini, 2014). Our modeling shows that the motion of crustal material over the basement sheet B ramp focuses 5–8 km of exhumation in this region resetting cooling signals in a westward younging pattern.

As stated in section 1, different cross section geometries (particularly basement geometries) would impart different predicted cooling ages (Figure 16). In the following we describe how the pattern of cooling ages and basement deformation in three proposed crustal cross sections (Baby et al., 1997; McQuarrie et al., 2008; Müller et al., 2002) would differ. The primary influence of basement structures on cooling ages is that basement ramps focus exhumation (and thereby the location of the youngest ages) at different locations across a section, as well as over different widths across the section (i.e., narrow versus distributed exhumation above the basement structures). In Figure 16, we show the modeled cooling ages for the McQuarrie et al. (2008) section and hypothesize what the predicted cooling ages may look like for crustal sections from Baby et al. (1997) and Müller et al. (2002) based on the geometry of the basement structures and a 50 Ma start of deformation. For example, in the crustal cross section of Baby et al. (1997), a 20 km thick stack of repeating eastward verging and eastward younging basement thrust faults is proposed. With this geometry and the patterns in cooling ages over structures gleaned from section 4, we would expect that the oldest ages would be above the western most ramp, located at the western edge of the EC (Figure 16b) and that the ages would get younger over each successive ramp toward the east. Similar to our section (Figure 16a), the amount of SAZ displacement is tied to the amount of displacement on the hanging wall and footwall of the youngest ramp. Thus, the youngest predicted cooling ages would be located at the top of that ramp, and be associated with motion on the SAZ (Figures 16a and 16b). A key difference is that the Baby et al. (1997) active basement ramp is shallow (~15°) and long (~ 60 km), and thus, the vertical component of rock uplift, erosion, and cooling associated with it would be lower than our geometry, and the width of reset ages broader (cf. Lock & Willett, 2008). This difference in basement geometry is reflected in the different patterns of cooling ages (compared cooling ages over EC in Figures 16a and 16b). As a second example, the interpreted basement geometry of Müller et al. (2002) is shown in Figure 16c. In this geometry, the basement faults range in thickness from 8 to 15 km and verge both to the east (in the eastern EC and IAZ) and west (western EC). The colocation of both the early east verging EC ramp and the SAZ ramp (Figure 16c) would suggest the deepest exhumation of reset cooling ages there (orange line Figure 16c), as well as the youngest lower temperature chronometers (blue and green lines Figure 16c). The younger component of exhumation will also make the ages recorded by deeper exhumed cooling ages younger than their initial cooling age (e.g., Figures 8 and 16). The predicted ages imparted by the basement thrusts would be the youngest in the center (where ramps of both east and west verging basement faults are focused) and get older to the west (with the west verging basement faults) and to the east (with the east verging basement faults). Only the rocks that have not been uplifted by basement faults (western most EC and SAZ) will have cooling age signals that track motion on smaller offset thrust faults in Paleozoic and younger rocks (Figure 16c).

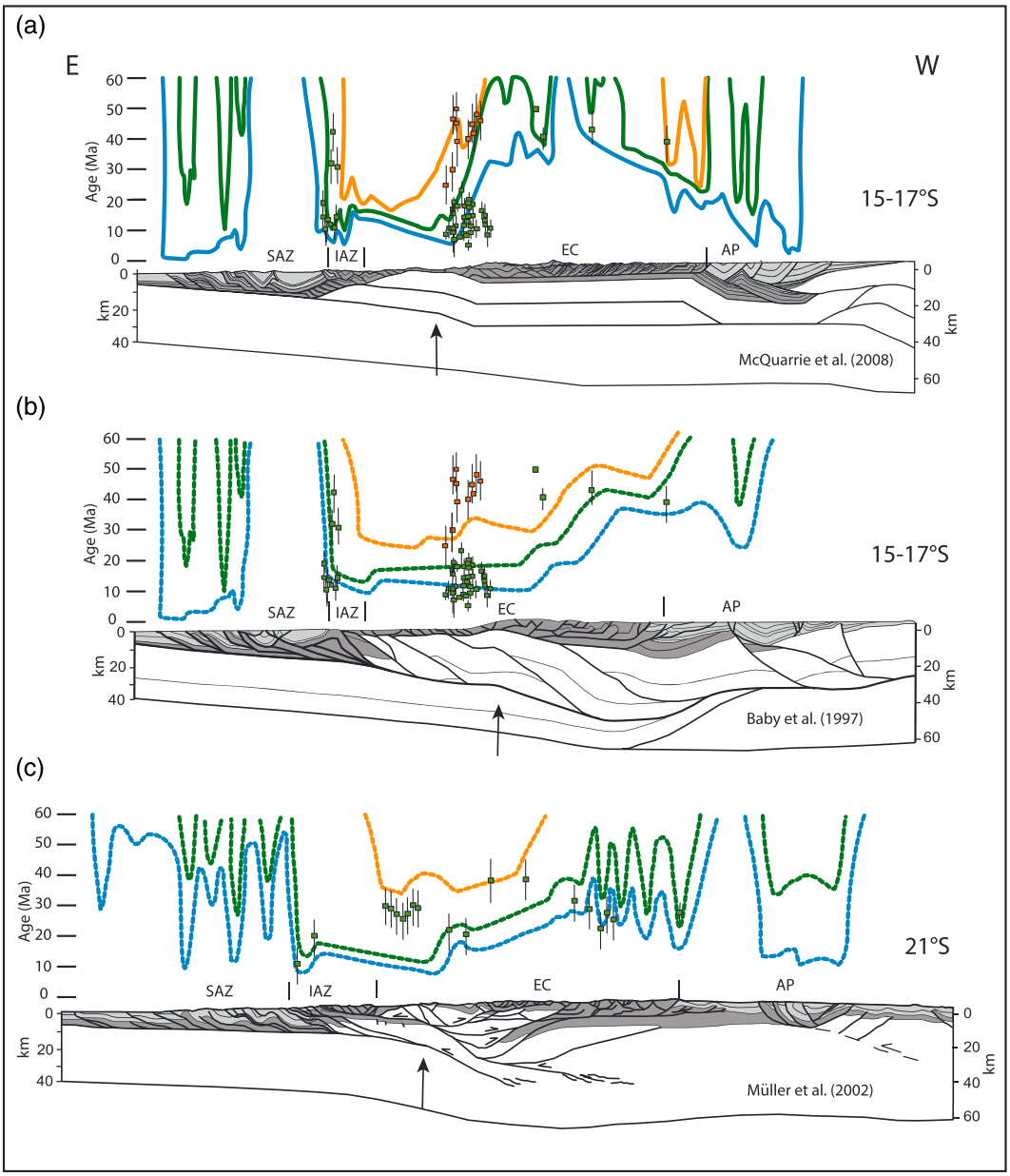

Figure 16. Mechanisms for basement accommodation of shortening in the Bolivian Andes, (a) predicted or (b, c) hypothesized thermochronometer cooling patterns based on basement structure and kinematics, and published thermochronometer ages in the EC and IAZ. Cross sections are from McQuarrie et al. (2008) (Figure 16a), Baby et al. (1997) (Figure 16b), and Müller et al. (2002) (Figure 16c). Thermochronometer ages (2σ error) are from the compilation presented in this study (Figures 16a and 16b; see supporting information Tables SI 1 and SI 2) and Scheuber et al. (2006) (Figure 16c). Arrows indicate the top of the youngest (active) footwall ramp. Similarities in all three sections include basement thrust faults (8–20 km thick) that accommodate tens of kilometers of displacement and account for abrupt changes in structural elevation. Key differences are the location of basement ramps and the kinematics of deformation. The predicted (solid) and hypothesized (dashed) age curves are based on assuming a 50 Ma start to deformation and a constant deformation rate. Predicted ages for Figure 16a show the effect of full SAZ sedimentation on cooling signal in the SAZ (ES scenario) but the misalignment of predicted (green line) and measured (green squares) AFT ages in the eastern EC because the basement ramp proposed by McQuarrie et al. (2008) is too far east. Hypothesized ages for Figure 16b match the western AFT ages (due to the 50 Ma start), but the age of basement thrusting gets younger to the east. We suggest that the younger age of each successive thrust sheet and the additional uplift over the youngest SAZ ramp would result in predicted cooling ages (orange dashed line) that are too young to match the 45–35 Ma ZFT ages in the EC (orange squares). The overlap of at least three west verging footwall ramps and two east verging footwall ramps in Figure 16c will promote the maximum amount of uplift, exhumation, and young ages in the center of the EC, even though the proposed start of deformation is 50 Ma. The colocation of two, 10 km high footwall ramps, the youngest of which accommodates SAZ deformation, suggests that the predicted AFT cooling ages from the IAZ to the western edge of the active ramp should be young (~15–8 Ma).

For all three cross sections in Figure 16, the predicted cooling ages in the IAZ match the age that deformation initiated in the SAZ with cooling ages that young to the west as a function of the eastern basement thrust sheet moving up and over a ramp. The distinguishing signal between these different basement geometries is the predicted age of cooling in the EC. Baby et al. (1997) requires that the western EC ages are the oldest and get younger to the east. The Müller et al. (2002) section requires EC cooling ages associated with basement deformation to be youngest in the center and get older to the east and the west in the direction of transport. The McQuarrie et al. (2008) section predicts the oldest ages are in the center of the EC and young toward the ramps in the east and west.

5.2. Cooling Signal Imparted by Basin Subsidence

Deposition of cold, low-conductivity sediments advects isotherms downward in sedimentary basins thereby decreasing thermal gradients (Carslaw & Jaeger, 1959; Husson & Moretti, 2002; Lucazeau & Le Douran, 1985). Modeling studies have shown that even moderate sedimentation rates (~0.2 mm/yr) lower the heat flow in sedimentary basins (Ehlers, 2005; Theissen & Rüpke, 2009). The thermochronometric modeling presented here indicates different exhumation magnitudes are necessary to reset the same thermochronometer based on the location of the sample in the FTB-FB system, and the associated foreland basin history. For example, AFT samples in the EC backthrust belt that are never covered with significant FB sediment are partially reset with as little as 3.4 km of exhumation (Figure 8b) and fully reset with 4 km of exhumation (Figure 8c). However, in the SAZ with no imposed subsidence (and thus smaller foreland basins), 4 km of exhumation just starts partial resetting of the eastern most AFT system in the SAZ (easternmost SAZ thrust sheet Figure 7h). When a long-wavelength subsidence is imposed, the subsidence magnitude is increased and foreland basin thicknesses and subsequent exhumation magnitudes experienced by samples later exposed at the surface must increase as well. However, even with the increased magnitudes of exhumation (5.7–6.0 km), the predicted ages still show partial resetting of the AFT system (Figure 12) because active sedimentation cools the geothermal gradient. The predicted AFT ages in the SAZ become fully reset only when including early subsidence, slow SAZ deformation (17–19.5 Ma initiation of SAZ deformation), and higher heat production (Ao = 0.7). The slower rate and longer window of time for sedimentation allows crustal heating to keep pace with sedimentation. Due to this effect, velocity models with low rates of deformation (and sedimentation) predict increased appearance of reset AFT ages in SAZ thrust sheets (Figure 13).

5.3. Long-Wavelength Imposed Uplift and Subsidence

The discrepancy between the thickness of measured FB fill in the SAZ to the thickness of modeled FB strata produced solely by thrust loads highlights the need for alternative subsidence mechanisms. When accounting for sediment load in subsidence models (using thrust and sediment loads of 2,400 kg/m^3 with an EET of 75 km) only a 3% increase in basin depth was observed when compared to the parameters used without accounting for sediment load (thrust loads of 2,900 kg/m^3 and no sediment load, with an EET of 75 km) (Figure 5) (section 3.1 and supporting information section S2). We suggest that the discrepancy between the magnitude of FB subsidence produced by viable thrust loads and EET ($<$5 km) and the observed depth of the SAZ basins (7 km) indicates the presence of dynamic subsidence in this region. In addition, in a purely flexural system, topographic elevation is obtained and maintained by thrust faulting. Once thrust faulting ceases in the region, that region gradually subsides with time due to loading from uplift along distal ramps. Thus, modeled elevations in the EC decrease slowly through time and do not match modern EC elevations mandating imposed uplift to match the modern elevation profile.

In retroarc FB systems, dynamic subsidence, related to viscous coupling of the mantle wedge, can increase the load experienced by the foreland, facilitate the increased preservation of FB sediment and alter the depth and location of FB deposits (Catuneanu, 2004; Davila et al., 2007; DeCelles, 2012; Gurnis, 1993; Mitrovica et al., 1989). Accumulation of sedimentary packages in the North American Cordillera strongly suggests a component of dynamic subsidence in addition to flexural subsidence related to thrust-fault loading (Gurnis, 1992, 1993; Painter et al., 2013). Subsidence of 200–300 m was imposed on the model in the Beni synclines during selected deformation steps adding 2 km of increased subsidence (supporting information Figure S2) during SAZ deformation to reproduce the thickness and extent of post-Oligocene basin fill.

Imposed uplift in the EC and AP was necessary to maintain the high elevations present in the hinterland of the Andes today. Several arguments against flexural support of the Andean Plateau have been proposed

including Airy isostatic compensation due to a thick crustal column (Beck et al., 1996), the presence of weak lower crust (Isacks, 1988), delamination processes invoking recent (<4 Ma) rapid uplift (Garzione et al., 2006; Babeyko & Sobolev, 2005), and thickening of the EC and AP by lower crustal material displaced to the west due to SAZ shortening (Eichelberger et al., 2015; Husson & Sempere, 2003; Isacks, 1988; Lamb, 2011). Crustal thicknesses of ~70 km beneath the AP are consistent with Airy-type isostasy indicating the high elevations in the hinterland are supported by thick crust and not the EET of the lithosphere (Beck et al., 1996). Additionally, the high magnitude of documented upper crustal shortening in the Bolivian Andes (Eichelberger et al., 2013; McQuarrie, 2002a; McQuarrie et al., 2008) must be balanced by lower crustal shortening (not specifically modeled in this study) and thickening producing an excess of lower crust that must be accounted for (e.g., delamination or lower crustal flow) (Eichelberger & McQuarrie, 2015; Garzione et al., 2006; Leier et al., 2013). Since these processes responsible for the modern elevation of the hinterland of the Bolivian Andes cannot be flexurally modeled, an approximately 500 m imposed uplift in the EC and AP is implemented during selected steps of SAZ deformation to reproduce the modern topographic expression of the FTB and maintain high elevation in the hinterland (supporting information Figure S2). This vertical adjustment does not change the relationship of modeled particle paths to the surface but only changes the absolute elevation of the hinterland in the model after the initiation of imposed uplift. Cooling ages from models with EC and AP imposed uplift are nearly identical when compared with the same model without the hinterland adjustment and are driven by surface temperature differences due to the model atmospheric lapse rate.

5.4. Comparison of Modeled Deformation Rates to Published Data

The sensitivity of modeled thermochronologic data to the age at which deformation initiates indicates that northern Bolivian EC started deforming at 50–55 Ma. This initiation age is largely insensitive to the basement geometry (Figure 16) in that basement deformation in the northern Bolivia EC would need to initiate early enough to produce the measured 45–50 Ma cooling ages regardless of geometry (Figure 8 and Tables SI 1 and SI 2). This initiation date is >15 Ma earlier than interpretations that dominantly rely on synorogenic sediment data (Allmendinger et al., 1997; Jordan et al., 1997; Sempere et al., 1990). When modeling a sequentially deforming FTB and an evolving FB system, it becomes apparent that sediments shed from the earliest deformational phases are rarely preserved in the associated FB systems, especially if shortening magnitudes are large (DeCelles, 2012). Therefore, synorogenic sediment ages in FTB systems should not be interpreted as indicators of the initiation of deformation. However, when combined with cross section kinematics and associated FB evolution models that calculate thrust loads, and the resulting age, location, and thickness of basins, dated synorogenic sedimentary rocks provide critical age constraints on deformation.

The early initiation of crustal shortening suggested in this study also predates deformation age predictions made using AFT, ZFT, K/Ar, and $^{40}Ar/^{39}Ar$ thermochronometer cooling ages from Triassic plutons exhumed in the EC (Benjamin et al., 1987; Farrar et al., 1988; Gillis et al., 2006). Age elevation plots were used to identify two ZFT trends that intersect at 45 Ma to argue for a change in exhumation rates at this time (Benjamin et al., 1987). Biotite and muscovite K/Ar dates and $^{40}Ar/^{39}Ar$ step heating of EC samples identified minimum age plateaus at 38 Ma which were interpreted as a regionally extensive (400 km along strike) thermal event associated with early deformation in the core of the EC (Farrar et al., 1988; McBride et al., 1987). More comprehensive analysis of $^{40}Ar/^{39}Ar$ and fission track thermochronology by Gillis et al. (2006) used the entire cooling path experienced by the samples to corroborate interpretations that cooling began at 45–40 Ma. Some amount of shortening is required to impose sufficient uplift, erosion, and exhumation to reset thermochronometer cooling signals in the EC (Figure 7b). The delay between the onset of deformation and oldest reset ZFT age is 8 Ma in the 50 Ma constant velocity model (Figure 7h).

Rates of deformation in the northern Bolivian Andes are sensitive to the proposed cross-section geometry and magnitude of shortening. The acceptable velocity envelope for the Beni modeled section (Figure 15) shows that for this cross section, both constant rates of shortening through time (5–6 mm/yr), as well as periods of rapid shortening (9–12 mm/yr) interspersed with slow shortening rates (2–3 mm/yr) fit measured cooling ages. A period of rapid deformation is permissible when deformation initiates at ~50–55 Ma and peaks at 45 Ma. This rapid shortening must be followed by slow deformation rates from 40 to 15 Ma with rates increasing at ~15 Ma and peaking at 10–12 Ma. Initiation of deformation in the SAZ is linked to the initial motion of basement thrust sheet B (Figure 7g). Motion on this basement thrust sheet forces exhumation above the hanging and footwall ramps and results in focused exhumation in the IAZ and westward

migrating exhumation in the EC (Figures 7g and 7h). The 10–14 Ma cooling ages in the IAZ and easternmost EC require basement-induced exhumation at or immediately preceding these ages. In addition, erosion of Mesozoic through Ordovician strata at the eastern edge of the EC (interpreted as a result of motion on basement sheet B) must predate the deposition of the Cangalli Formation at 9–7 Ma. Constant rates of shortening with SAZ initiating at 17–19.5 Ma with a rate of 5–6 mm/yr fit these constraints (Figure 11). Early SAZ deformation at 18–20 Ma is consistent with previous HeFTy modeling indicating rapid exhumation between 4 Ma and 19 Ma (Barnes et al., 2006; McQuarrie et al., 2008). Models with variable deformation rates require rapid deformation (9–12 mm/yr) soon after the initiation of SAZ shortening between 15 and 12 Ma to match both the IAZ exhumation and the Cangalli Formation deposition constraints.

Using the Baby et al. (1997) shortening model, deformation initiating at 50 Ma would produce a shortening rate of 3–3.5 mm/yr from 50 to 20–15 Ma. Because the westernmost basement thrust and associated deformation in the Paleozoic rocks above it deform first, Salla synorogenic sedimentation does not limit deformation continuing in the eastern EC post 25 Ma in the Baby et al. (1997) section; however, a 50–25 Ma window of EC and IAZ deformation would increase shortening rates to 4 mm/yr. The age and rate of SAZ shortening is limited by the same constraints used to model shortening in this study. Initiation of SAZ deformation in the Baby et al. (1997) section would uplift the eastern most EC and IAZ and trigger exhumation there. This SAZ deformation could initiate as early as 20 Ma or as late as 13 Ma and suggests rates of 3.7 to 5.7 mm/yr.

The proposed elevated rates of shortening during SAZ deformation (9–12 mm/yr) falls within the range of modern GPS rates of shortening in the SAZ (9–13 mm/yr) (Bevis et al., 2001; Brooks et al., 2011; Klotz et al., 2001) and geologic rates determined for the SAZ in southern Bolivia that fluctuate between 0–5 mm/yr and 11–13 mm/yr from 9 Ma to present (Echavarria et al., 2003). In contrast, acceptable SAZ start dates from the velocity models range from 20 to 13 Ma, 11 to 4 Ma older than the 9 Ma start date suggested by Echavarria et al. (2003) from sediment accumulation curves in southern Bolivia. Young AHe samples from the SAZ that record rapid exhumation at 6 ± 2 Ma are also used to argue for a young start to SAZ deformation (Lease et al., 2016); however, this period of rapid exhumation is accurately predicted by all velocity models tested because it is a function of the final motion of material over a SAZ footwall ramp that occurs in all models between 7.5 and 5.5 Ma. A 15 Ma start date, with rates of shortening peaking around 11 Ma, may be a function of orographically enhanced exhumation (Barnes et al., 2012) linked to attainment of threshold elevations ($>$75% of modern, Ehlers & Poulsen, 2009). The increase SAZ shortening rates would facilitate replacing eroded material in the deforming SAZ wedge and thus enable the westward motion of the basement decollement ramp. Erosion above the newly developed basement thrust sheet ramp (B) at the initiation of SAZ shortening links exhumation signals in the IAZ and EC to SAZ thrust sheet emplacement and SAZ deformation. The age and location of this exhumation is the cooling signal that is most sensitive to the age and rate of SAZ deformation (Figures 12–14).

Previous estimates of shortening rates are based on total shortening magnitudes and the estimated age over which that shortening occurred. Using a section across southern Bolivia (Figures 16, 21°S) and combining cross section shortening estimates, synorogenic sediment accumulation curves preserved in the SAZ and AFT cooling ages, Oncken et al. (2006) proposed shortening rates that varied through time (Figure 17a orange line; Oncken et al., 2006). The proposed shortening rates are strongly influenced by Oligocene (Sempere et al., 1990) and Miocene synorogenic deposits (Uba et al., 2006), as well as AFT data across the EC and IAZ in southern Bolivia that range from 40 to 20 Ma, (Figure 16) (Scheuber et al., 2006). Emphasis on the Oligocene basin deposits combined with the aerial extent of the 30–20 Ma AFT ages lead the authors to propose high shortening rates during the Oligocene. SAZ shortening magnitude was quantified at 21°S (90 km) but the age of shortening was taken from the well-dated section at 22.5°S, where 60 km of shortening occurs over the last 9 million years (Echavarria et al., 2003). Due to these factors, the strain accumulation model (Oncken et al., 2006) underpredicts rates of shortening from 55–50 Ma to 33 Ma and overpredicts rates of shortening from 33 Ma to 15 Ma and 8 Ma to the present when compared to the acceptable shortening rate envelope for northern Bolivia (15–17°S)(Figure 17a). Although this strain accumulation model is centered 500 km south of our modeled section, the hypothetical cooling curves in Figure 16 (assuming a 50 Ma start of deformation), compared to the cooling data from the region, highlight potential conflicts between the proposed shortening rates, the geometry of the cross section, and the cooling data from the region.

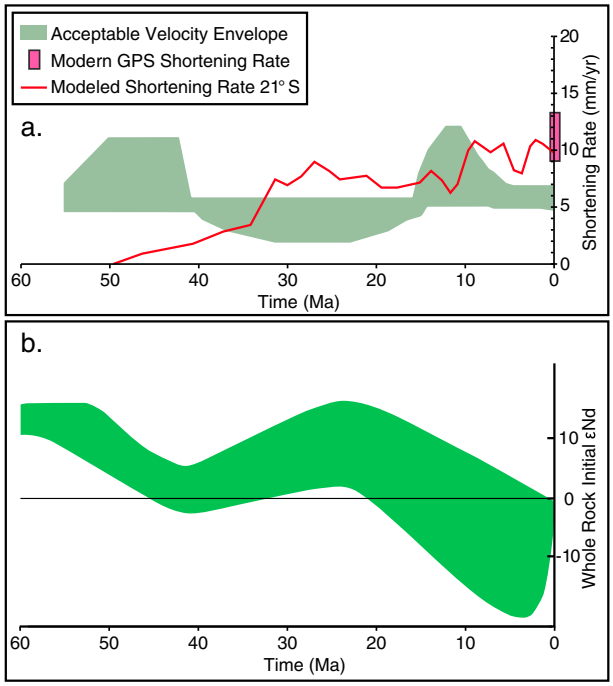

Figure 17. (a) Shortening rate diagram with acceptable shortening rate envelope (this study), modern GPS rates of shortening (pink box) (Bevis et al., 2001; Klotz et al., 2001), and modeled shortening rate from 21°S (red line; Oncken et al., 2006). (b) Whole rock εNd values for the Bolivian Andes volcanic rocks over the past 60 Ma (DeCelles et al., 2009).

5.5. Cyclicity in Cordilleran Systems

Episodes of rapid shortening separated by periods of limited compression to possibly extension were some of the original models proposed for Andean orogenesis (e.g., Mégard, 1984; Mégard et al., 1984; Noble et al., 1974; Steinmann, 1929) and based primarily on structural and stratigraphic relationships in the Peruvian Andes. These observations lead to named periods of deformation such as Incaic (~45–40 Ma), Quechua 1 (~20–17 Ma), Quechua 2 (~10–8 Ma), and Quechua 3 (6–4 Ma) (Mégard et al., 1984) and drove research directed at finding correlation (or lack thereof) between proposed pulses of deformation and plate tectonic drivers (e.g., Jaillard & Soler, 1996; Pardo-Casas & Molnar, 1987; Somoza & Ghidella, 2012). More recently, a cyclicity (alternating rapid and sluggish shortening), inherent to Cordilleran systems, was proposed based on observations that suggest upper and lower crustal processes work in conjunction to impact magmatism, shortening rates, sediment accumulation, and orogenic isostasy (DeCelles et al., 2009; DeCelles & Graham, 2015). The proposed model begins with normal arc magmatism followed by an increase in retroarc shortening that feeds lowermost continental lithosphere beneath the arc. The influx of continental material seeds high-flux magmatism with strongly negative εNd ratios and is hypothesized to leave a dense melt residue that may promote delamination and rapid elevation gain. Times of dense residue accumulation promote subcritical taper angles potentially limiting FTB propagation while rapid delamination induced uplift and resulting supercritical angles would promote deformation to jump toward the foreland (DeCelles et al., 2009). Cyclicity in these processes is suggested by oscillations in the concentration of εNd (Figure 17b; DeCelles et al., 2009). DeCelles et al. (2009) use the Oncken et al. (2006) shortening rate curve to argue for a 25–40 Myr delay between periods of rapid shortening and the resulting change in arc composition. Comparing the Oncken et al. (2006) shortening rate curve to the values of εNd with time, rapid shortening occurs while εNd values are high, necessitating the long lag time for the resulting change in arc composition. Our revised rates of shortening provide a stronger support for the proposed cyclicity. The peak shortening rates (48 Ma and 11 Ma) precede the lowest measured εNd value by ~8 Myr (Figure 17). Conversely, εNd values increase during periods of decreased shortening rates.

6. Conclusion

This research focuses on how the geometry and kinematics of balanced cross sections can be used as inputs for isostatic and thermochronometric models. Application of these coupled models provides a test for the viability of proposed cross section geometry, constraints on the timing and rates of shortening, and insights into the evolution of a FTB-FB system.

The method of deriving particle paths for thermokinematic models from sequentially deformed, isostatically compensated, balanced cross sections facilitates the creation of an integrated model that predicts both thermochronometer cooling in the FTB and the ages of modeled sediment in adjacent FB. The location of a basement thrust ramp proposed by McQuarrie et al. (2008) resulted in a mismatch between predicted and measured AFT cooling ages in the EC prompting the development of an alternate cross-section geometry and kinematics. The revised kinematic model results in a modest increase in shortening (285 km) versus the original 276 km proposed in the original balanced cross section (McQuarrie et al., 2008). This new cross-section geometry moved the basement ramp ~14 km to the west and significantly improved the match of predicted and observed AFT ages.

Insufficiently thick predicted SAZ basin deposits and predicted EC elevations that were significantly lower than modern elevations produced in the first iteration of flexural models highlighted the need for long-wavelength subsidence in the foreland and uplift in the hinterland. The need for this imposed subsidence

argues that a significant component of dynamic subsidence resulting from viscous coupling between the mantle wedge and the subducting oceanic plate (DeCelles, 2012) influenced the central Andean foreland, particularly over the last 20–30 Myr. Imposed uplift in the hinterland may be related to the attainment of Airy isostasy (Beck et al., 1996), via lower crustal flow (Eichelberger et al., 2015; Lamb, 2011), delamination rebound (Garzione et al., 2008), or a combination of both.

Model-predicted thermochronometer cooling patterns indicate that deformation initiated in the EC at 50–55 Ma, earlier than previously inferred. An early initiation is needed to reproduce EC 40–50 Ma AFT and 38–46 Ma ZFT sample ages in the EC, and to correctly predict the age of synorogenic sedimentary deposits. A set of constant and variable rate deformation models were found to reproduce thermochronologic and geochronologic constraints along the modeled cross section. These were combined to define an acceptable rate of shortening envelope where the first pulse of shortening initiated around 50–55 Ma, peaked around 48–45 Ma, and was followed by a period of decreased shortening rates. A second pulse of rapid shortening that defines acceptable SAZ rates, initiated between 15 and 13 Ma and peaked at 11–10 Ma before rapidly declining. While these periods of rapid shortening are remarkably similar to the Incaic (~45–40 Ma) and Quechua 2 (~10–8 Ma) orogenic phases proposed by Mégard (e.g., Mégard, 1984; Mégard et al., 1984), we stress that these potential windows of more rapid shortening are separated by times of much slower deformation (2–5 mm/yr) consistent with the idea of cordilleran cyclicity (DeCelles et al., 2009), but counter to the hypothesis that compressional stresses were absent or replaced by extension (Mégard et al., 1984). Initiation of SAZ deformation is ~15 Ma in most acceptable velocity models but may have occurred as early as 20 Ma, or as recent as 13 Ma. The initiation of SAZ deformation determined in this study is concurrent with proposed ages of SAZ initiation in Peru (Espurt et al., 2011; Eude et al., 2015; Perez et al., 2016); however, the age is 4–11 Myr earlier than ages identified in southern Bolivia (9 Ma, Echavarria et al., 2003), which are often used in geodynamical models of the South American Cordillera (DeCelles et al., 2009; Garzione et al., 2008).

Acknowledgments
We thank the four anonymous reviewers and Associate Editor Jolivet for constructive comments that improved earlier versions of this manuscript. Supporting data are included in the supporting information file; any additional data or information are available through contacting N. McQuarrie; the modified version of Pecube that can be coupled to 2-D Move restoration files is available through T. A. Ehlers; and the compiled data for this paper can be obtained from Adam Rak (e-mail: adam.rak.geo@gmail.com). This work was supported NSF by grant EAR 0908972 to N. M. and European Research Council grant ERC-CoG 715703 to T. A. E. This manuscript benefit from thoughtful discussions over the years with Nathan Eichelberger, Michelle Gilmore, Brian Horton, Richard Lease, and Nicholas Perez. Willi Kappler (University of Tübingen) is thanked for support with conducting modeling simulations.

References

Allmendinger, R. W., Jordan, T. E., Kay, S. M., & Isacks, B. L. (1997). The evolution of the Altiplano-Puna Plateau of the central Andes. *Annual Review of Earth and Planetary Sciences*, *25*(1), 139–174. https://doi.org/10.1146/annurev.earth.25.1.139

Arndt, J., Bartel, T., Scheuber, E., & Schilling, F. (1997). Thermal and rheological properties of granioritic rocks from the Central Andes, North Chile. *Tectonophysics*, *271*(1-2), 75–88. https://doi.org/10.1016/S0040-1951(96)00218-1

Armijo, R., Lacassin, R., Coudurier-Curveur, A., & Carrizo, D. (2015). Coupled tectonic evolution of Andean Orogeny and global climate. *Earth-Science Reviews*, *143*, 1–35. https://doi.org/10.1016/j.earscirev.2015.01.005

Babeyko, A. Y., & Sobolev, S. V. (2005). Quantifying different modes of the late Cenozoic shorting in the central Andes. *Geology*, *33*(8), 621–624. https://doi.org/1130/G21126.1

Baby, P., Limachi, R., Moretti, I., Mendez, E., Oller, J., Guiller, B., & Specht, M. (1995). Petroleum system of the northern and central Bolivian sub-Andean zone. In A. J. Tankard, R. Suarez, & H. J. Welsink (Eds.), *Petroleum Basins of South America*, *American Mem. AAPG* (Vol. 62, pp. 445–458).

Baby, P., Rochat, P., Mascle, G., & Hérail, G. (1997). Neogene shortening contribution to crustal thickening in the back arc of the central Andes. *Geology*, *25*(10), 883–886. https://doi.org/10.1130/0091-7613(1997)025%3C0883:NSCTCT%3E2.3.CO;2

Barnes, J. B., & Ehlers, T. A. (2009). End member models for Andean Plateau uplift. *Earth-Science Reviews*, *97*(1-4), 105–132. https://doi.org/10.1016/j.earscirev.2009.08.003

Barnes, J. B., Ehlers, T. A., Insel, N., McQuarrie, N., & Paulsen, C. J. (2012). Linking orography, climate, and exhumation across the Central Andes. *Geology*, *40*(12), 1135–1138. https://doi.org/10.1130/G33229.1

Barnes, J. B., Ehlers, T. A., McQuarrie, N., O'Sullivan, P. B., & Pelletier, J. D. (2006). Variations in Eocene to recent erosion across the central Andean fold-thrust belt, northern Bolivia: Implications for plateau evolution. *Earth and Planetary Science Letters*, *248*(1-2), 118–133. https://doi.org/10.1016/j.epsl.2006.05.018

Beck, S. L., Zandt, G., Myers, S. C., Wallace, T. C., Silver, P. G., & Drake, L. (1996). Crustal thickness variations in the central Andes. *Geology*, *24*(5), 407–410. https://doi.org/10.1130/0091-7613(1996)024%3C0407:CTVITC%3E2.3.CO;2

Benjamin, M. T., Johnson, N. M., & Naeser, C. W. (1987). Recent rapid uplift in the Bolivian Andes; evidence from fission-track dating. *Geology*, *15*(7), 680–683. https://doi.org/10.1130/0091-7613(1987)15%3C680:RRUITB%3E2.0.CO;2

Bevis, M., Kendrick, E., Smalley, R., Jr., Brooks, B., Allmendinger, R., & Isacks, B. (2001). On the strength of interpolate coupling and the rate of back arc convergence in the central Andes: An analysis of the interseismic velocity field. *Geochemistry, Geophysics, Geosystems*, *2*(11), 1067. https://doi.org/10.1029/2001GC000198

Boyer, S. E. (1995). Sedimentary basin taper as a factor controlling the geometry and advance of thrust belts. *American Journal of Science*, *295*, 1220–1254. https://doi.org/10.2475/ajs.295.10.1220

Braun, J. (2003). Pecube: A new finite-element code to solve the 3D heat transport equation including the effects of a time-varying, finite amplitude surface topography. *Computers & Geosciences*, *29*(6), 787–794. https://doi.org/10.1016/S0098-3004(03)00052-9

Braun, J. (2005). Quantifying constraints on the rate of landform evolution from low-temperature thermochronology. In P. W. Reiners & T. A. Ehlers (Eds.), *Low-Temperature Thermochronology: Techniques, Interpretations and Applications*. *Min. Soc. Am. Rev. Min. Geochem.* (Vol. 58, pp. 351–374). https://doi.org/10.2138/rmg.2005.58.13

Brooks, A. B., Bevis, M., Whipple, K., Arrowsmith, J. R., Foster, J., Zapata, T., … Smalley, R. J. Jr. (2011). Orogenic-wedge deformation and potential for great earthquakes in the central Andes backarc. *Nature Geoscience Letters*, *4*(6), 380–383. https://doi.org/10.1038/NGE01143

Carslaw, H. S., & Jaeger, J. C. (1959). *Conduction of Heat in Solids* (2nd ed., 520 pp.). Oxford, UK: Oxford University Press.
Catuneanu, O. (2004). Retroarc foreland systems—Evolution through time. *Journal of African Earth Sciences*, *38*(3), 225–242. https://doi.org/10.1016/j.jafrearsci.2004.01.004
Coney, P. J., & Evenchick, C. A. (1994). Consolidation of the American Cordillersas. *Journal of South American Earth Sciences*, *7*(3-4), 241–262. https://doi.org/10.1016/0895-9811(94)90011-6
Dahlen, F. A. (1990). Critical taper models of fold-and-thrust belts and accretionary wedges. *Annual Review of Earth and Planetary Sciences*, *18*, 55–99.
Davila, F. M., Astini, R. A., Jordan, T. E., Gehrels, G., & Ezpeleta, M. (2007). Miocene forebulge development previous to the broken foreland partitioning in the southern Central Andes, west-central Argentina. *Tectonics*, *26*, TC5016. https://doi.org/10.1029/2007TC002118
DeCelles, P. G. (2012). Foreland basin systems revisited: Variations in response to tectonic setting. In C. Busby & A. Azor (Eds.), *Tectonics of Sedimentary Basins* (1st ed., pp. 405–426). Oxford, UK: Blackwell. https://doi.org/10.1002/9781444347166.ch20
DeCelles, P. G., Ducea, M. N., Kapp, P., & Zandt, G. (2009). Cyclicity in cordilleran orogenic systems. *Nature Geoscience*, *2*(4), 251–257. https://doi.org/10.1038/NGEO469
DeCelles, P. G., & Graham, S. A. (2015). Cyclical processes in the North American Cordilleran orogenic system. *Geology*, *43*(6), 499–502. https://doi.org/10.1130/G36482.1
DeCelles, P. G., & Horton, B. K. (2003). Early to middle Tertiary foreland basin development and the history of Andean crustal shortening in Bolivia. *Geological Society of America Bulletin*, *115*(1), 58–77. https://doi.org/10.1130/0016-7606(2003)115%3C0058:ETMTFB%3E2.0.CO;2
Deutscher Wetterdient (1991). Climate panel of Santa Cruz, Bolivia, 1952-1990, 1.
Dunn, J. F., Hartshorn, K. G., & Hartshorn, P. W. (1995). Structural styles and hydrocarbon potential of the sub-Andean thrust belt of southern Bolivia. In A. J. Tankard, R. Suarez, & H. J. Welsink (Eds.), *Petroleum Basins of South America*, *Mem. AAPG* (Vol. 62, pp. 523–543).
Echavarria, L., Hernandez, R., Allmendinger, R., & Reynolds, J. (2003). Subandean thrust and fold belt of northwestern Argentina: Geometry and timing of the Andean evolution. *American Association of Petroleum Bulletin*, *87*(6), 965–985. https://doi.org/10.1306/01200300196
Ehlers, T. A. (2005). Crustal thermal processes and thermochronometer interpretations. *Reviews in Mineralogy and Geochemistry*, *58*(1), 315–350. https://doi.org/10.2138/rmg.2005.58.12
Ehlers, T. A., Chaudhri, T., Kumar, S., Fuller, C. W., Willett, S. D., Ketcham, R., … Fu, F. (2005). Computational tools for low-temperature thermochronometer interpretation. *Reviews in Mineralogy and Geochemistry*, *58*(1), 589–622. https://doi.org/10.2138/rmg.2005.58.22
Ehlers, T. A., & Poulsen, C. J. (2009). Influence of Andean uplift on climate and paleoaltimetry estimates. *Earth and Planetary Science Letters*, *281*(3-4), 238–248. https://doi.org/10.1016/j.epsl.2009.02.026
Eichelberger, N., & McQuarrie, N. (2015). Kinematic reconstruction of the Bolivian Orocline. *Geosphere*, *11*(2), 445–462. https://doi.org/10.1130/GES01064.1
Eichelberger, N., McQuarrie, N., Ryan, J., Karimi, B., Beck, S., & Zandt, G. (2015). Evolution of crustal thickening in the central Andes Bolivia. *Earth and Planetary Science Letters*, *426*, 191–203. https://doi.org/10.1016/j.epsl.2015.06.035
Eichelberger, N., McQuarrie, N., Ehlers, T. A., Enkelmann, E., Barnes, J. B., & Lease, R. O. (2013). New constraints on the chronology, magnitude, and distribution of deformation within the central Andean orocline. *Tectonophysics*, *32*(5), 1432–1453. https://doi.org/10.1002/tect.20073
Espurt, N., Barbarand, J., Roddaz, M., Brusset, S., Baby, P., Saillard, M., & Hermoza, W. (2011). A scenario for late Neogene Andean shortening transfer in the Camisea Subandean zone (Peru, 12°S): Implications for growth of the northern Andean Plateau. *Geologic Society of America Bulletin*, *123*, 2050–2068. https://doi.org/10.1130/B30165.1
Eude, A., Roddaz, M., Brichau, S., Brusset, S., Calderon, Y., Baby, P., & Soula, J. C. (2015). Controls on timing of exhumation and deformation in the northern Peruvian eastern Andean wedge as inferred from low-temperature thermochronology and balanced cross section. *Tectonics*, *34*, 715–730. https://doi.org/10.1002/2014TC003641
Farrar, E., Clark, A. H., Kontak, D. J., & Archibald, D. A. (1988). Zongo-San Gaban Zone: Eocene foreland boundary of the central Andean orogen, northwest Bolivia and southeast Peru. *Geology*, *16*(1), 55–58. https://doi.org/10.1130/0091-7613(1988)016%3C0055:ZSGNZE%3E2.3.CO;2
Garzione, C. N., Hoke, G. D., Libarkin, J. C., Withers, S., MacFadden, B., Eiler, J., … Mulch, A. (2008). Rise of the Andes. *Science*, *320*(5881), 1304–1307. https://doi.org/10.1126/science.1148615
Garzione, C. N., Molnar, P., Libarkin, J., & MacFadden, B. (2006). Rapid late Miocene rise of the Bolivian Altiplano: Evidence for removal of mantle lithosphere. *Earth and Planetary Science Letters*, *241*(3-4), 543–556. https://doi.org/10.1016/j.epsl.2005.11.026
Geobol (1994a). Carta Geologica de Bolivia, Chulumani (Hoja 6044), [Servicio Geologico de Bolivia], La Paz (scale 1:100,000).
Geobol (1994b). Carta Geologica de Bolivia, Coroico (Hoja 6045), [Servicio Geologico de Bolivia], La Paz (scale 1:100,000).
Geobol (1995a). Carta Geologica de Bolivia, Calamarca (Hoja 5943), [Servicio Geologico de Bolivia], La Paz (scale 1:100,000).
Geobol (1995b). Carta Geologica de Bolivia, Sapahaqui (Hoja 6043), [Servicio Geologico de Bolivia], La Paz (scale 1:100,000).
Geobol (1996). Mapas tematicos de recursos minerales de Bolivia, Corocoro y Charana, [Servicio Geologico de Bolivia], La Paz (scale 1:250,000).
Geobol (1997). Mapas tematicos de recursos minerales de Bolivia, La Paz y Copacabana, [Servicio Geologico de Bolivia], La Paz (scale 1:250,000).
Gillis, R. J., Horton, B. K., & Grove, M. (2006). Thermochronology, geochronology, and upper crustal structure of the Cordillera Real: Implications for Cenozoic exhumation of the central Andean plateau. *Tectonics*, *25*, TC6007. https://doi.org/10.1029/2005TC001887
Gonfiantini, R., Roche, M. A., Olivry, J. C., Fontes, J. C., & Zuppi, G. M. (2001). The altitude effect on the isotopic composition of tropical rains. *Chemical Geology*, *181*(1-4), 147–167. https://doi.org/10.1016/S0009-2541(01)00279-0
Gotberg, N., McQuarrie, N., & Caillaux, V. C. (2010). Comparison of crustal thickening budget and shortening estimates in southern Peru (12–14°S): Implications for mass balance and rotations in the "Bolivian orocline". *Geological Society of America Bulletin*, *122*(5-6), 727–742. https://doi.org/10.1130/B26477.1
Gurnis, M. (1992). Rapid continental subsidence following the initiation and evolution of subduction. *Science*, *255*(5051), 1556–1558. https://doi.org/10.1126/science.255.5051.1556
Gurnis, M. (1993). Depressed continental hypsometry behind oceanic trenches: A clue to subduction controls on sea-level change. *Geology*, *21*(1), 29–32. https://doi.org/10.1130/0091-7613(1993)021%3C0029:DCHBOT%3E2.3.CO;2
Hampton, B. A., & Horton, B. K. (2007). Sheet flow processes in a rapidly subsiding basin, Altiplano plateau, Bolivia. *Sedimentology*, *54*(5), 1121–1148. https://doi.org/10.111/j.1365-3091.2007.00875.x
Hamza, V. M., Silva Dias, F. J. S., Gomes, A. J. L., & Delgadilho Terceros, Z. G. (2005). Numerical and functional representations of regional heat flow in South America. *Physics of the Earth and Planetary Interiors*, *152*(4), 223–256. https://doi.org/10.1016/j.pepi.2005.04.009
Hatcher, R. D., & Hooper, R. J. (1992). Evolution of crystalline thrust sheets in the internal parts of mountain chains. In K. R. McClay (Ed.), *Thrust Tectonics* (pp. 217–233). London: Chapman and Hall. https://doi.org/10.1007/978-94-011-3066-0_20

Hindle, D., Kley, J., Klosko, E., Stein, S., Dixon, T., & Norabuena, E. (2002). Consistency of geologic and geodetic displacements during Andean orogenesis, *Geophysical Research Letters*, *29*(8), 1188. https://doi.org/10.1029/2001GL013757

Hoke, G. D., & Garzione, C. N. (2008). Paleosurfaces, paleoelevation, and the mechanisms for the late Miocene topographic development of the Altiplano plateau. *Earth and Planetary Science Letters*, *271*(1-4), 192–201. https://doi.org/10.1016/j.epsl.2008.04.008

Horton, B. K. (1999). Erosional controls on the geometry and kinematics of thrust belt development in the central Andes. *Tectonics*, *18*(6), 1292–1304. https://doi.org/10.1029/1999TC900051

Horton, B. K. (2005). Revised deformation history of the central Andes: Inferences from Cenozoic foredeep and intermontane basins of the Eastern Cordillera, Bolivia. *Tectonics*, *24*, TC3011. https://doi.org/10.1029/2003TC001619

Horton, B. K. (2012). Cenozoic evolution of hinterland basins in the Andes and Tibet. In C. Busby & A. Azor (Eds.), *Tectonics of Sedimentary Basins* (1st ed., pp. 427–444). Oxford, UK: Blackwell. https://doi.org/10.1002/9781444347166.ch21

Horton, B. K., & DeCelles, P. G. (1997). The modern foreland basin system adjacent to the Central Andes. *Geology*, *25*(10), 895–898. https://doi.org/10.1130/0091-7613(1997)025%3C0895:TMFBSA%3E2.3.CO;2

Horton, B. K., Hampton, B. A., LAReau, B. N., & Baldellon, E. (2002). Tertiary provenance history of the northern and central Altiplano (Central Andes, Bolivia): A detrital record of plateau-margin tectonics. *Journal of Sedimentary Research*, *72*(5), 711–726. https://doi.org/10.1306/020702720711

Horton, B. K., Hampton, B. A., & Waanders, G. L. (2001). Paleogene synorogenic sedimentation in the Altiplano plateau and implications for initial mountain building in the central Andes. *Geological Society of America Bulletin*, *113*(11), 1387–1400. https://doi.org/10.1130/0016-7606(2001)113%3C1387:PSSITA%3E2.0.CO;2

Husson, L., & Moretti, I. (2002). Thermal regime of fold and thrust belts—An application to the Bolivian sub Andean zone. *Tectonophysics*, *345*(1-4), 253–280. https://doi.org/10.1016/S0040-1951(01)00216-5

Husson, L., & Sempere, T. (2003). Thickening the Altiplano crust by gravity-driven crustal channel flow. *Geophysical Research Letters*, *30*(5), 1243. https://doi.org/10.1029/2002GL016877

Iaffaldano, G., Bunge, H. P., & Dixon, T. H. (2006). Feedback between mountain belt growth and plate convergence. *Geology*, *34*(10), 893–896. https://doi.org/10.1130/G22661.1

Isacks, B. L. (1988). Uplift of the Central Andean Plateau and bending of the Bolivian orocline. *Journal of Geophysical Research*, *93*(B4), 3211–3231. https://doi.org/10.1029/JB093iB04p03211

Jaillard, E., & Soler, P. (1996). Cretaceous to Paleogene tectonic evolution of the northern Central Andes (0–18°S) and its relations to geodynamics. *Tectonophysics*, *259*(1-3), 41–53. https://doi.org/10.1016/0040-1951(95)00107-7

James, D. E., & Sacks, S. (1999). Cenozoic formation of the Central Andes: A geophysical perspective. In B. Skinner, et al. (Eds.), *Geology and Mineral Deposits of Central Andes*. *Society of Economic Geologists Special Publication* (Vol. 7, pp. 1–25).

Jordan, T. E. (1981). Thrust loads and foreland basin evolution, Cretaceous, western United States. *American Association of Petroleum Geologists Bulletin*, *65*, 12.

Jordan, T. E. (1995). Retroarc foreland and related basins. In C. J. Busby & R. V. Ingersoll (Eds.), *Tectonics of Sedimentary Basins* (pp. 331–362). Oxford, UK: Blackwell.

Jordan, T. E., Reynolds, J. H. III, & Erikson, J. P. (1997). Variability in age of initial shortening and uplift in the central Andes, 16–33°30′S. In W. F. Ruddiman (Ed.), *Tectonic Uplift and Climate Change* (pp. 41–46). New York: Plenum Press. https://doi.org/10.1007/978-1-4615-5935-1_3

Kay, R. F., MacFadden, B. J., Madden, R. H., Sandeman, H., & Anaya, F. (1998). Revised age of the Salla beds, Bolivia, and its bearing on the age of the Deseadan South American land mammal "age". *Journal of Vertebrate Paleontology*, *18*(1), 189–199. https://doi.org/10.1080/02724634.1998.10011043

Kennan, L., Lamb, S., & Rundle, C. (1995). K-Ar dates from the Altiplano and Cordillera Oriental of Bolivia: Implications for Cenozoic stratigraphy and tectonics. *Journal of South American Earth Sciences*, *8*(2), 163–186. https://doi.org/10.1016/0895-9811(95)00003-X

Kley, J. (1996). Transition from basement-involved to thin-skinned thrusting in the Cordillera Oriental of southern Bolivia. *Tectonics*, *15*(4), 763–775. https://doi.org/10.1029/95TC03868

Kley, J. (1999). Geologic and geometric constraints on a kinematic model of the Bolivian Orocline. In K. J. Reutter (Ed.), *Central Andean Deformation* (pp. 221–235). Oxford, UK: Pergamon.

Kley, J., Gangui, A. H., & Kruger, D. (1996). Basement involved blind thrusting in the eastern Cordillera Oriental, southern Bolivia: Evidence from cross-sectional balancing, gravimetric and magnetotelluric data. *Tectonophysics*, *259*, 179–184.

Kley, J., & Monaldi, C. (1998). Tectonic shortening and crustal thickening in the central Andes: How good is the correlation? *Geology*, *26*(8), 723–726. https://doi.org/10.1130/0091-7613(1998)026%3C0723:TSACTI%3E2.3.CO;2

Kley, J., Monaldi, C., & Salfity, J. A. (1999). Along-strike segmentation of the Andean foreland, causes and consequences. *Tectonophysics*, *301*(1-2), 75–94. https://doi.org/10.1016/S0040-1951(98)90223-2

Klotz, J., Khazaradze, G., Angermann, D., Reigber, C., Perdomo, R., & Cifuentes, O. (2001). Earthquake cycle dominates contemporary crustal deformation in Central and Southern Andes. *Earth and Planetary Science*, *193*(3-4), 437–446. https://doi.org/10.1016/S0012-821X(01)00532-5

Lamb, S. (2011). Did shortening in thick crust cause rapid Late Cenozoic uplift in the northern Bolivian Andes. *Journal of the Geological Society of London*, *168*(5), 1079–1092. https://doi.org/10.1144/0016-76492011-008

Lamb, S., & Hoke, L. (1997). Origin of the high plateau in the Central Andes, Bolivia, South America. *Tectonics*, *16*(4), 623–649. https://doi.org/10.1029/97TC00495

Lamb, S., Hoke, L., Kennan, L., & Dewey, J. (1997). Cenozoic evolution of the Central Andes in Bolivia and northern Chile. In J. P. Burg & M. Ford (Eds.), *Orogeny Through Time*, *Special Publication* (Vol. 121, pp. 237–264). London: Geological Society.

Lease, R. O., & Ehlers, T. A. (2013). Incision into the eastern Andean Plateau during Pliocene cooling. *Science*, *341*(6147), 774–776. https://doi.org/10.1126/science.1239132

Lease, R. O., Ehlers, T. A., & Enkelmann, E. (2016). Large along-strike variations in the onset of Subandean exhumation: Implications for Central Andean orogenic growth. *Earth and Planetary Science Letters*, *451*, 62–76. https://doi.org/10.1016/j.epsl.2016.07.004

Leier, A., McQuarrie, N., Garzione, C., & Eiler, J. (2013). Stable isotope evidence for multiple pulses of rapid surface uplift in the Central Andes, Bolivia. *Earth and Planetary Science Letters*, *371-372*, 49–58. https://doi.org/10.1016/j.epsl.2013.04.025

Leier, A., McQuarrie, N., Horton, B. K., & Gehrels, G. E. (2010). Upper Oligocene conglomerates of the Altiplano, Central Andes: The record of deposition and deformation along the margin of a hinterland basin. *Journal of Sedimentary Research*, *80*(8), 750–762. https://doi.org/10.2110/jsr.2010.064

Lock, J., & Willett, S. (2008). Low-temperature thermochronometric ages in fold-and-thrust belts. *Tectonophysics*, *456*(3-4), 147–162. https://doi.org/10.1016/j.tecto.2008.03.007

Lucassen, F., Beccio, R., Harmon, R., Kasemann, S., Franz, G., Trumbull, R., … Dulski, P. (2001). Composition and density model of the continental crust at an active continental margin—The Central Andes between 21° and 27°S. *Tectonophysics*, *341*(1-4), 195–223. https://doi.org/10.1016/S0040-1951(01)00188-3

Lucazeau, F., & Le Douran, S. (1985). The blanketing effect of sedimentation in basins formed by extension: A numerical model. Application to the Gulf of Lyon Viking graben. *Earth and Planetary Science Letters*, *74*(1), 92–102. https://doi.org/10.1016/0012-821X(85)90169-4

MacFadden, B. J., Campbell, K. E., Cifelli, R. L., Siles, O., Johnson, N. M., Naeser, C. W., & Zeitler, P. K. (1985). Magnetic polarity stratigraphy and mammalian fauna of the Deseadan (late Oligocene–early Miocene) Salla Beds of northern Bolivia. *Journal of Geology*, *93*(3), 223–250. https://doi.org/10.1086/628950

Marshall, L. G., Swisher, C. C. III, Lavenu, A., Hoffstetter, R., & Curtis, G. H. (1992). Geochronology of the mammal-bearing late Cenozoic on the northern Altiplano, Bolivia. *Journal of South American Earth Sciences*, *5*(1), 1–19. https://doi.org/10.1016/0895-9811(92)90056-5

Masek, J. G., Isacks, B. L., Gubbels, T. L., & Fielding, E. J. (1994). Erosion and tectonics at the margins of continental plateaus. *Journal of Geophysical Research*, *99*(B7), 13,941–13,956. https://doi.org/10.1029/94JB00461

McBride, S. L., Clark, A. H., Farrar, E., & Archibald, D. A. (1987). Delimitation of a cryptic Eocene tectono-thermal domain in the Eastern Cordillera of the Bolivian Andes through K-Ar dating and ^{40}Ar-^{39}Ar step-heating. *Journal of the Geological Society, London*, *144*(2), 243–255. https://doi.org/10.1144/gsjgs.144.2.0243

McFadden, B. J., Campbell, K. E., Ciffelli, R. L., Siles, O., Johnson, N. M., Naeser, C. W., & Zeitler, P. K. (1985). Magnetic polarity stratigraphy and mammalian fauna of the Deseadan (late Oligocene–early Miocene) Salla beds of northern Bolivia. *Journal of Geology*, *93*, 233–250.

McQuarrie, N. (2002a). The kinematic history of the central Andean fold–thrust belt, Bolivia: Implications for building a high plateau. *Geological Society of America Bulletin*, *114*(8), 950–963. https://doi.org/10.1130/0016-7606(2002)114%3C0950:TKHOTC%3E2.0.CO;2

McQuarrie, N. (2002b). Initial plate geometry, shortening variations, and evolution of the Bolivian orocline. *Geology*, *30*(10), 867–870. https://doi.org/10.1130/0091-7613(2002)030%3C0867:IPGSVA%3E2.0.CO;2

McQuarrie, N., Barnes, J. B., & Ehlers, T. A. (2008). Geometric, kinematic, and erosional history of the central Andean Plateau, Bolivia (15–17 °S). *Tectonics*, *27*, TC3007. https://doi.org/10.1029/2006TC002054

McQuarrie, N., & DeCelles, P. (2001). Geometry and structural evolution of the Central Andean back thrust belt, Bolivia. *Tectonics*, *20*(5), 669–692. https://doi.org/10.1029/2000TC001232

McQuarrie, N., & Ehlers, T. A. (2015). Influence of thrust belt geometry and shortening on thermochronometer cooling ages: Insights form thermokinematic and erosion modeling of the Bhutan Himalaya. *Tectonics*, *34*, 1055–1079. https://doi.org/10.1002/2014TC003783

McQuarrie, N., & Ehlers, T. A. (2017). Techniques for understanding fold-and-thrust belt kinematics and thermal evolution. In *Linkages and Feedbacks in Orogenic Systems*, *Geological Society of America Memoir* (Vol. 213, pp. 1–30). https://doi.org/10.1130/2017.1213(02)

McQuarrie, N., Horton, B. K., Zandt, G., Beck, S., & DeCelles, P. G. (2005). Lithospheric evolution of the Andean fold-thrust belt, Bolivia, and the origin of the central Andean plateau. *Tectonophysics*, *399*(1-4), 15–37. https://doi.org/10.1016/j.tecto.2004.12.013

McRae, L. (1990). Paleomagnetic isochrones, unsteadiness, and uniformity of sedimentation in Miocene intermontane basin sediments at Salla, Eastern Andean Cordillera, Bolivia. *Journal of Geology*, *98*(4), 479–500. https://doi.org/10.1086/629420

Meade, B. J., & Conrad, C. P. (2008). Andean growth and the deceleration of South America subduction: Time evolution of a coupled orogen-subduction system. *Earth and Planetary Science Letters*, *275*(1-2), 93–101. https://doi.org/10.1016/j.epsl.2008.08.007

Mégard, F. (1984). The Andean orogenic period and its major structures in central and northern Peru. *Journal of the Geological Society of London*, *141*(5), 893–900. https://doi.org/10.1144/gsjgs.141.5.0893

Mégard, F., Noble, D. C., McKee, E. H., & Bellon, H. (1984). Multiple pulses of Neogene compressive deformation in the Ayacucho intermontane basin, Andes of central Peru. *Geological Society of America Bulletin*, *95*(9), 1108–1117. https://doi.org/10.1130/0016-7606(1984)95%3C1108:MPONCD%3E2.0.CO;2

Mitra, G. (1997). Evolution of salients in a fold-and-thrust belt: The effects of sedimentary basin geometry, strain distribution and critical taper. In S. Sengupta (Ed.), *Evolution of Geological Structures in Micro- to Macroscales* (pp. 59–90). London: Chapman and Hall.

Mitrovica, J. X., Beaumont, C., & Jarvis, G. T. (1989). Tilting of continental interiors by the dynamical effects of subduction. *Tectonics*, *8*(5), 1079–1094. https://doi.org/10.1029/TC008i005p01079

Mosolf, J. G., Horton, B. K., Heizler, M. T., & Matos, R. (2011). Unroofing the core of the central Andean fold-thrust belt during the focused late Miocene exhumation; evidence from the Tipuani-Mapiri wedge-top basin, Bolivia. *Basin Research*, *23*(3), 346–360. https://doi.org/10.1111/j.1365-2117.2010.00491.x

Mount, V. S. (2014). Structural style of the Appalachian Plateau fold belt, north-central Pennsylvania. *Journal of Structural Geology*, *69*, 284–303. https://doi.org/10.1016/j.jsg.2014.04.005

Müller, J. P., Kley, J., & Jacobshagen, V. (2002). Structure and Cenozoic kinematics of the Eastern Cordillera, southern Bolivia (21°S). *Tectonics*, *21*(5), 1-1–1-24. https://doi.org/10.1029/2001TC001340

Murray, B. P., Horton, B. K., Matos, R., & Heizler, M. T. (2010). Oligocene-Miocene basin evolution in the northern Altiplano, Bolivia: Implications for evolution of the central Andean backthrust belt and high plateau. *American Association of Petroleum Geologists Bulletin*, *122*(9-10), 1443–1462. https://doi.org/10.1130/B30129.1

Noble, D. C., McKee, E. H., Farrar, E., & Petersen, U. (1974). Episodic Cenozoic volcanism and tectonism in the Andes of Peru. *Earth and Planetary Science Letters*, *21*(2), 213–220. https://doi.org/10.1016/0012-821X(74)90057-0

Norton, K., & Schlunegger, F. (2011). Migrating deformation in the Central Andes from enhanced orographic rain-fall. *Nature Communications*, *2*, 584. https://doi.org/10.1038/ncomms1590

Oncken, O., Hindle, D., Kley, J., Kirsten, E., Victor, P., & Schemmann, K. (2006). Deformation of the central Andean upper place system—Facts, fiction, and constraints for plateau models. In O. Oncken, et al. (Eds.), *The Andes Active Subduction Orogeny* (pp. 3–27). New York: Springer.

Painter, C. S., Carrapa, B., DeCelles, P. G., Gehrels, G. E., & Thomson, S. N. (2013). Exhumation of the North American Cordillera revealed by multi-dating of Upper Jurassic-Upper Cretaceous foreland basin deposits. *Geological Society of America Bulletin*, *126*(11-12), 1439–1464. https://doi.org/10.1130/B30999.1

Pardo-Casas, F., & Molnar, P. (1987). Relative motion of the Nazca (Farallon) and South American plates since Late Cretaceous time. *Tectonics*, *6*(3), 233–248. https://doi.org/10.1029/TC006i003p00233

Perez, N. D., Horton, B. K., McQuarrie, N., Stübner, K., & Ehlers, T. A. (2016). Andean shortening, inversion and exhumation associated with thin- and thick-skinned deformation in southern Peru. *Geological Magazine*, *153*, 1013–1041. https://doi.org/10.1017/S0016756816000121

Rahn, M. K., & Grasemann, B. (1999). Fission track and numerical thermal modeling of differential exhumation of the Glarus thrust plane (Switzerland). *Earth and Planetary Science Letters*, *169*(3-4), 245–259. https://doi.org/10.1016/S0012-821X(99)00078-3

Ramos, V. A., & Folguera, A. (2009). Andean flat-slab subduction through time. In J. B. Murphy, J. D. Keppie, & A. J. Hynes (Eds.), *Ancient Orogens and Modern Analogues*, *Special Publication* (Vol. 327, pp. 31–54). London: Geologic Society.

Rodriguez, G., & Fernando, W. (2002). Evolution lateral de la deformacion de un frente origenico, ejemplo de las cuencas subandinas entre 0°Y 16°S, Sociedad Geologica Del Peru, Institut de recherché pour le developpement (IRD), Publicacion Especial N° 4, 129.

Ryan, J., Beck, S., Zandt, G., Wagner, L., & Minaya, E. (2016). Central Andean crustal structure from receiver function analysis. *Tectonphisics*, *682*, 120–133. https://doi.org/10.1016/j.tecto.2016.04.048

Safran, E. B., Blythe, A. E., & Dunne, T. (2006). Spatially variable exhumation rates in orogenic belts: An Andean example. *Journal of Geology*, *114*(6), 665–681. https://doi.org/10.1086/507613

Sandeman, H. A., Clark, A. H., & Farrar, E. (1995). An integrated tectono-magmatic model for the evolution of the Southern Peruvian Andes (13°–20°S) since 55 Ma. *International Geology Review*, *37*(12), 1039–1073. https://doi.org/10.1080/00206819509465439

Scheuber, E., Mertmann, D., Ege, H., Silva-Gonzalez, P., Heubeck, C., Reutter, K.-J., & Jacobshagen, V. (2006). Exhumation and basin development related to formation of the central Andean plateau, 21°S. In O. Oncken et al. (Eds.), *The Andes Active Subduction Orogeny* (pp. 296–312). New York: Springer.

Sempere, T., Butler, R. F., Richards, D. R., Marshall, L. G., Sharp, W., & Swisher, C. C. III (1997). Stratigraphy and chronology of Upper Cretaceous-lower Paleogene strata in Bolivia and northwest Argentina. *Geological Society of America Bulletin*, *109*(6), 709–727. https://doi.org/10.1130/0016-7606(1997)109%3C0709:SACOUC%3E2.3.CO;2

Sempere, T., Herail, G., Oller, J., & Bonhomme, M. G. (1990). Late Oligocene–early Miocene major tectonic crisis and related basins in Bolivia. *Geology*, *18*(10), 946–949. https://doi.org/10.1130/0091-7613(1990)018%3C0946:LOEMMT%3E2.3.CO;2

Sheffels, B. (1990). Lower bound on the amount of crustal shortening in the central Bolivian Andes. *Geology*, *18*(9), 812–815. https://doi.org/10.1130/0091-7613(1990)018%3C0812:LBOTAO%3E2.3.CO;2

Shi, Y., & Wang, C. (1987). Two-dimensional modeling of the *P-T-t* paths of regional metamorphism in simple overthrust terrains. *Geology*, *15*(11), 1048–1051. https://doi.org/10.1130/0091-7613(1987)15%3C1048:TMOTPP%3E2.0.CO;2

Somoza, R., & Ghidella, M. E. (2012). Late Cretaceous to recent plate motions in western South America revisited. *Earth and Planetary Science Letters*, *331-332*, 152–163. https://doi.org/10.1016/j.epsl.2012.03.003

Song, Y., Zhao, M., Liu, S., Hong, F., & Fang, S. (2010). Oil and gas accumulation in the foreland basins, central and western China. *Acta Geologica Sinica*, *84*(2), 382–405. https://doi.org/10.1111/j.1755-6724.2010.00151.x

Springer, M. (1999). Interpretation of heat-flow density in the Central Andes. *Tectonophysics*, *306*(3-4), 377–395. https://doi.org/10.1016/S0040-1951(99)00067-0

Steinmann, G. (1929). *Geologie Von Peru* (448 pp.). Heidelberg, Germany: Karl Winter.

Stockmal, G. S., Beaumont, C., Nguyen, M., & Lee, B., (2007). Mechanics of thin-skinned fold-and-thrust belts: Insights from numerical models. In J. W. Sears, et al. (Eds.), *Whence the Mountains? Inquiries into the Evolution of Orogenic Systems: A Volume in Honor of Raymond A. Price*. *Geological Society of America Special Paper, 433*, 63–98. https://oi.org/10.1130/2007.2433

Syracuse, E. M., van Keken, P. E., & Abers, G. A. (2010). The global range of subduction zone thermal models. *Physics of the Earth and Planetary Interiors*, *183*(1-2), 73–90. https://doi.org/10.1016/j.pepi.2010.02.004

Tassara, A. (2005). Interaction between the Nasca and South American Plates and formation of the Altiplano-Puna plteau: Review of a flexural analysis along the Andean margin (15°–34°S). *Geochemistry, Geophysics, Geosystems*, *7*, Q01001. https://doi.org/10.1029/2005GC001040

Theissen, S., & Rüpke, L. H. (2009). Feedbacks of sedimentation on crustal heat flow: New insights from the Vøring Basin, Norwegian Sea. *Basin Research*, *22*, 976–990. https://doi.org/10.1111/j.1365-2117.2009.00437.x

Uba, C. E., Heubeck, C., & Hulka, C. (2006). Evolution of the late Cenozoic Chaco foreland basin, Southern Bolivia. *Basin Research*, *18*(2), 145–170. https://doi.org/10.1111/j.1365-2117.2006.00291

Watts, A. B., Lamb, S. H., Fairhead, J. D., & Dewey, J. F. (1995). Lithospheric flexure and bending of the central Andes. *Earth and Planetary Science Letters*, *134*, 9–21. https://doi.org/10.1016/0012-821X(95)00095-T

Whipp, D. M. Jr., Ehlers, T. A., Braun, J., & Spath, C. D. (2009). Effects of exhumation kinematics and topographic evolution on detrital thermochronometer data. *Journal of Geophysical Research*, *114*, F04021. https://doi.org/10.1029/2008JF001195

Whipple, C., & Gasparini, N. (2014). Tectonic control of topography, rainfall patterns, and erosion during rapid post-12 uplift of the Bolivian Andes. *Lithosphere*, *6*(4), 251–268. https://doi.org/10.1130/L325.1

Zubieta Rossetti, D., Baby, P., & Mugnier, J. L. (1996). Cenozoic evolution of the Andean foreland basin between 15°30′ and 22°00′S. In *Extended Abstracts, Third International Symposium on Andean Geodynamics* (pp. 529–532). St. Malo, France: Paris, ORSTOM.